

1 Three-dimensional spatio-angular fluorescence
2 microscopy with a polarized dual-view inverted
3 selective-plane illumination microscope
4 (pol-diSPIM)

5 Talon Chandler^{1,2*†}, Min Guo^{3,4*†}, Yijun Su^{4,5,6}, Jiji Chen⁵,
6 Yicong Wu⁴, Junyu Liu³, Atharva Agashe⁷, Robert S. Fischer⁸,
7 Shalin B. Mehta^{1,2,9}, Abhishek Kumar⁹, Tobias I. Baskin^{10,11},
8 Valentin Jamouille^{8,12}, Huafeng Liu³, Vinay Swaminathan^{13,14},
9 Amrinder Nain^{7,15}, Rudolf Oldenbourg⁹, Patrick La Rivière^{2,11},
10 Hari Shroff^{4,5,6,11}

11 ¹CZ Biohub SF, San Francisco, 94158, California, USA.

12 ²Department of Radiology, University of Chicago, Chicago, 60637,
13 Illinois, USA.

14 ³State Key Laboratory of Extreme Photonics and Instrumentation,
15 College of Optical Science and Engineering, Zhejiang University,
16 Hangzhou, 310027, Zhejiang, China.

17 ⁴Laboratory of High Resolution Optical Imaging, National Institute of
18 Biomedical Imaging and Bioengineering, National Institutes of Health,
19 Bethesda, 20892, Maryland, USA.

20 ⁵Advanced Imaging and Microscopy Resource, National Institutes of
21 Health, Bethesda, 20892, Maryland, USA.

22 ⁶Janelia Research Campus, Howard Hughes Medical Institute, Ashburn,
23 20147, Virginia, USA.

24 ⁷Department of Mechanical Engineering, Virginia Tech, Blacksburg,
25 24061, Virginia, USA.

26 ⁸Cell Biology and Physiology Center, National Heart, Lung, and Blood
27 Institute, National Institutes of Health, Bethesda, 20892, Maryland,
28 USA.

29 ⁹Bell Center, Marine Biological Laboratory, Woods Hole, 02543,
30 Massachusetts, USA.

31 ¹⁰Biology Department, University of Massachusetts, Amherst, 01003,
32 Maryland, USA.

33 ¹¹Whitman Center, Marine Biological Laboratory, Woods Hole, 02543,
34 Massachusetts, USA.

35 ¹²Department of Molecular Biology and Biochemistry, Simon Fraser
36 University, Burnaby, V5A 1S6, British Columbia, Canada.

37 ¹³Department of Clinical Sciences, Lund University, Lund, SE-221 00,
38 Scania, Sweden.

39 ¹⁴Wallenberg Centre for Molecular Medicine, Lund University, Lund,
40 SE-221 00, Scania, Sweden.

41 ¹⁵Department of Biomedical Engineering and Mechanics, Virginia Tech,
42 Blacksburg, 24061, Virginia, USA.

43 *Corresponding author(s). E-mail(s): talon.chandler@czbiohub.org;
44 guom@zju.edu.cn;

45 †These authors contributed equally to this work.

46 **Abstract**

47 Polarized fluorescence microscopy is a valuable tool for measuring molecular
48 orientations, but techniques for recovering three-dimensional orientations and
49 positions of fluorescent ensembles are limited. We report a polarized dual-
50 view light-sheet system for determining the *three-dimensional orientations* and
51 diffraction-limited positions of ensembles of fluorescent dipoles that label biolog-
52 ical structures, and we share a set of visualization, histogram, and profiling tools
53 for interpreting these positions and orientations. We model our samples, their
54 excitation, and their detection using coarse-grained representations we call *orien-*
55 *tation distribution functions* (ODFs). We apply ODFs to create physics-informed
56 models of image formation with spatio-angular point-spread and transfer func-
57 tions. We use theory and experiment to conclude that light-sheet tilting is a
58 necessary part of our design for recovering all three-dimensional orientations.
59 We use our system to extend known two-dimensional results to three dimen-
60 sions in FM1-43-labelled giant unilamellar vesicles, fast-scarlet-labelled cellulose
61 in xylem cells, and phalloidin-labelled actin in U2OS cells. Additionally, we
62 observe phalloidin-labelled actin in mouse fibroblasts grown on grids of labelled
63 nanowires and identify correlations between local actin alignment and global
64 cell-scale orientation, indicating cellular coordination across length scales.

65 **Keywords:** light-sheet fluorescence microscopy, polarization, molecular orientation,
66 inverse problems

67 1 Introduction

68 Measuring the orientation of fluorescent molecules can provide valuable insights into
69 architecture, order, and dynamics in biology and material science [1]. By tagging a
70 biological structure with a fluorescent reporter that rotates along with the structure of
71 interest, biologists can deduce biophysical dynamics by measuring the orientation of
72 the fluorescent molecule. A large fraction of fluorescent reporters absorb and emit light
73 via an electronic dipole moment, i.e. in a polarized anisotropic pattern, so biologists
74 can use optical microscopy to examine a fluorophore’s excitation and emission patterns
75 to draw conclusions about the fluorescent reporter’s orientation.

76 Many techniques make *ensemble measurements* of diffraction-limited regions. By
77 making multiple measurements of the same region under variably polarized illumina-
78 tion and/or detection, then calculating each region’s *fluorescence anisotropy* [2, 3],
79 researchers can draw conclusions about membrane labelling [4, 5], septin dynamics
80 [6–8], nuclear pore proteins [9], force orientations [10, 11], and liquid crystals [12, 13].
81 Recent engineering efforts have improved the spatial resolution [14], signal-to-noise
82 ratio (SNR) [15], and out-of-plane resolution [16] of these ensemble measurements.
83 While some of these studies make assumptions about their samples to estimate three-
84 dimensional orientations, to our knowledge none simultaneously measure orientation
85 and position in three dimensions.

86 More recently, a collection of *single-molecule measurement* techniques has enabled
87 researchers to measure more parameters, including three-dimensional position, orien-
88 tation, and rotational dynamics, from a sparse set of emitters. These techniques have
89 been used to distinguish ordered and unordered biomolecular condensates [17], follow
90 DNA conformation changes under tension [18], and capture dynamics of amyloid fib-
91 rils [19], myosin [20], membrane [21], and actin [22, 23]. Despite considerable success,
92 these single-molecule efforts face challenges beyond those faced by all fluorescence
93 polarization techniques, with tighter constraints on throughput, SNR, and choice of
94 emitters, constraining their wider adoption.

95 After surveying the field, we identified an unmet need for measurements that can
96 be used to recover the three-dimensional orientation and position of fluorescent ensem-
97 bles. We reasoned that a dual-view light-sheet system [24] should provide an excellent
98 platform for measuring the orientation of fluorescent ensembles because of its two exci-
99 tation and detection arms, enabling diverse illumination and detection polarizations
100 alongside improved axial spatial resolution.

101 In our initial iteration, we added liquid crystal polarizers to both excitation arms of
102 an existing dual-view light sheet system and attempted to recover the predominant ori-
103 entation of fluorophores from within each diffraction-limited volume [25]. We found it
104 challenging to merge a single-molecule description of the image formation process with
105 the pixel-wise fluorescence anisotropy methods that are common in ensemble measure-
106 ments, and we were unable to resolve orientational ambiguities. Inspired by the success
107 of diffusion-tensor magnetic resonance imaging (dMRI) [26] and its high-angular res-
108 olution extensions [27], we developed a coarse-grained formalism for spatio-angular
109 fluorescence microscopy [28–30] that we applied to our instrument. The formalism led
110 us to a set of critical engineering insights:

- 111 • unlike dMRI, fluorescence microscopes are *spatio-angularly coupled*, i.e. the orienta-
112 tion of molecules affects the spatial point-response function,
- 113 • in addition to the widely known spatial diffraction limit, fluorescence microscopes
114 face *angular diffraction limits* set by the physics of dipolar excitation, dipolar
115 emission, and the microscope’s geometry, and
- 116 • our initial design had a *hole in its spatio-angular transfer function*, a null function,
117 which caused the observed orientational ambiguities.

118 In this article we describe the key element of our formalism, the orientation dis-
119 tribution function (ODF), and how we have used it to model our three-dimensional
120 spatio-angular fluorescence microscope. We use ODFs to formulate a forward model
121 that lets us identify spatio-angular holes in our designs. We introduce a solution, *light-*
122 *sheet tilting*, and we demonstrate that it resolves the ambiguity with the same number
123 of measurements. Subsequently, we describe our observations of membranes, cell walls,
124 and actin in cells grown on a coverslip and on grids of nanowires. We close by inspect-
125 ing spatio-angular correlations across length scales, and we discuss future directions
126 for this field.

127 2 Results

128 2.1 Orientation distribution functions (ODFs) are 129 coarse-grained models of fluorescent dipoles that label 130 biological structures

131 **Figure 1(a)** depicts the class of fluorescent objects that we are trying to recover—
132 extended objects containing ensembles of molecules that move and rotate in three
133 dimensions and whose spatial and orientational properties we wish to characterize
134 within diffraction-limited regions. Assuming that each molecule’s excitation and emis-
135 sion dipole moments are aligned—a reasonable approximation for many fluorophores
136 [31]—we can summarize each fluorophore with a single axis. We can further summarize
137 all of the molecules within a diffraction-limited region with an *object ODF*, a spher-
138 ical function that we depict as a surface with a radius proportional to the number
139 of dipoles oriented along each direction. Fluorescent dipoles that label structures are
140 caught in angular potentials where they rotate during a measurement, contributing
141 to the width and angular-diffusive smoothness of the corresponding ODF. Note that
142 fluorescent dipoles are excited and emit symmetrically about their dipole axes which
143 means that (1) we can depict their dipole moments as axes instead of vectors, and (2)
144 their corresponding ODFs are always antipodally symmetric.

145 Object ODFs can describe a wide range of realistic 3D dipole distributions (**Figure**
146 **1(b)**). For example, dipoles that rotate freely in solution have an isotropic (spherical)
147 ODF, dipoles that lie flat in the plane of a membrane have a pancake-shaped ODF
148 with more tightly constrained dipoles having correspondingly flatter ODFs, dipoles
149 that are oriented normal to a membrane have a dumbbell-shaped ODF with more
150 tightly constrained dipoles having correspondingly sharper ODFs, and dipoles that lie
151 parallel to multiple axes within a diffraction-limited region have a multi-lobed ODF.

152 We have developed a *quasi-static* model of fluorescent ensembles, where angular
153 diffusion during a measurement is included within each object ODF, and object ODFs
154 do not change during a measurement. While this model is reasonably accurate for
155 many polarized fluorescence experiments, it ignores effects from fluorescence lifetime,
156 saturation, and spatial diffusion among others. For a complete account of the assump-
157 tions leading to our quasi-static model of fluorescent ensembles, we direct readers to
158 **Supplement 5** and [30].

159 Our primary strategy for generating contrast between different object ODFs is
160 orientation-selective excitation (**Figure 1(c)**). Orientation-selective excitation uses
161 polarized light to excite a subset of an object ODF’s molecules, creating a distribution
162 of excited molecules that we call an excited ODF. Linearly polarized illumination
163 excites an ensemble of dipole absorbers with an efficiency that is proportional to $\cos^2 \theta$,
164 where θ is the angle between the illumination polarization axis and the excitation
165 dipole moment of individual fluorophores in the distribution. Hence, the excited ODF
166 is the product of the object ODF and the excitation’s $\cos^2 \theta$ efficiency. When more
167 molecules are excited, more fluorescence can be emitted and collected, so the largest
168 signals will come from object ODFs that are parallel to the illumination polarization.
169 Light is polarized perpendicular to its direction of propagation, so we preferentially
170 excite emitters whose dipole moments are perpendicular to the optical axis of the
171 excitation objective.

172 Once we have an excited ODF, we can use orientation-selective detection to gener-
173 ate more contrast (**Figure 1(d)**). Ensembles of excited fluorophores emit polarized
174 anisotropic patterns that report their underlying excited ODF. Many instruments use
175 polarization filters/splitters to probe these polarization patterns, but here we rely only
176 on the intensity anisotropy of the emission pattern—a $\sin^2 \phi$ intensity distribution
177 where ϕ is the angle between the emission dipole moment and the emission direction.
178 By detecting light with an objective that does not collect light from the entire half
179 space (numerical aperture < index of refraction), we preferentially detect emitters
180 whose dipole moments are perpendicular to the optical axis of the detection objective.
181 Therefore, we will measure the largest signals from excited ODFs that lie entirely in
182 the plane perpendicular to the detection objective’s optical axis.

183 A single ODF can be modelled mathematically as *a function on a sphere*, where the
184 value of the function along a specific direction corresponds to the number of dipoles
185 along that direction. This means that we can write arbitrary ODFs as $f(\hat{\mathbf{s}}_o)$, where
186 $\hat{\mathbf{s}}_o$ is a coordinate on a two-dimensional sphere \mathbb{S}^2 . For example, dipoles in solution
187 (**Figure 1(c)(ii)**) can be represented by a constant-valued function $f^{(\text{solution})}(\hat{\mathbf{s}}_o) = C$,
188 where C is constant, and the corresponding excited ODF (**Figure 1(c)(iii)**) can
189 be represented by $f^{(\text{excited})}(\hat{\mathbf{s}}_o) = C|\hat{\mathbf{s}}_o \cdot \hat{\mathbf{p}}|^2 = C \cos^2 \theta$, where $\hat{\mathbf{p}}$ is the illumination
190 polarization and θ is the angle between $\hat{\mathbf{s}}_o$ and $\hat{\mathbf{p}}$.

191 **2.2 Polarized dual-view light-sheet microscopy enables**
192 **selective excitation, selective detection, and reconstruction**
193 **of fluorescent ensembles**

194 In this section we use ODFs as a tool to describe our imaging system, its con-
195 trast generation mechanisms, its limits, our reconstruction algorithms, and our
196 visualizations.

197 **Figure 2(a)** summarizes our dual-view excitation and detection strategy. Our
198 core instrumentation (**Supplement 1.1**) consists of an asymmetric diSPIM frame
199 equipped with a pair of water immersion objectives, each capable of excitation and
200 detection [32].

201 We use an excitation-path MEMS mirror (**Supplement 1.2**) to illuminate the
202 sample with a light sheet from the 0.67 numerical aperture (NA) objective, detect the
203 emitted light with the 1.1 NA objective, then scan the sample through the stationary
204 light sheet to acquire an imaging volume. We repeat the acquisition with the objectives'
205 roles swapped, illuminating with the 1.1 NA objective and detecting with the 0.67 NA
206 objective.

207 We added a liquid crystal module to both excitation arms (**Supplement 1.2**),
208 enabling our choice of arbitrary transverse polarization illumination. Instead of
209 exploring all possible illumination polarizations, we restricted our possible choices
210 to six linear polarization states, maximizing contrast while still enabling two-fold
211 oversampling of the underlying signals (**Supplement 2.1**).

212 Our complete acquisition consists of a calibration procedure (**Supplement 3.2**)
213 and the following data acquisition loops from fastest to slowest (**Supplement 3.3**):
214 (xy) camera frame, (z) stage scan positions, (\mathbf{v}) views, (p) illumination polarization,
215 (c) colors, and (T) time points. Our fastest single-time point, single-color acquisition
216 consists of six volumes (three illumination polarizations per view) acquired within
217 3.6 seconds.

218 After deskewing (**Supplement 4.1**) and registering (**Supplement 4.2**) the raw
219 data, we collect our irradiance measurements into a single function $g_{pv}(\mathbf{r}_d)$, where p
220 is a polarization index, \mathbf{v} is a view index, and $\mathbf{r}_d \in \mathbb{R}^3$ is a three-dimensional detector
221 coordinate (**Supplement 5.1**). Next, we model the object that we are trying to
222 estimate, a spatial distribution of ODFs, as a function $f(\mathbf{r}_o, \hat{\mathbf{s}}_o)$, where $\mathbf{r}_o \in \mathbb{R}^3$ is a
223 three-dimensional object-space coordinate and $\hat{\mathbf{s}}_o \in \mathbb{S}^2$ is an orientation coordinate.
224 Finally, we model the relationship between our data and our object as a shift-invariant
225 integral transform

$$g_{pv}(\mathbf{r}_d) = \int_{\mathbb{R}^3} d\mathbf{r}_o \int_{\mathbb{S}^2} d\hat{\mathbf{s}}_o h_{pv}(\mathbf{r}_d - \mathbf{r}_o, \hat{\mathbf{s}}_o) f(\mathbf{r}_o, \hat{\mathbf{s}}_o), \quad (1)$$

226 where $h_{pv}(\mathbf{r}_d - \mathbf{r}_o, \hat{\mathbf{s}}_o)$ is a *spatio-angular point-response function* (compare with **Sup-**
227 **plement 5.8**, see **Supplement 5.1** for indices p and j). The key features of **Equation**
228 **1** are (1) *linearity*: doubling the number of fluorophore doubles the detected irradiance;
229 (2) *3D spatial shift-invariance*: a spatial shift of a fluorophore results in a spatial shift
230 of its irradiance response; and (3) *spatio-angular coupling*: the spatial point-response
231 function depends on the dipole orientation. In other words, $h_{pv}(\mathbf{r}_d - \mathbf{r}_o, \hat{\mathbf{s}}_o)$ cannot

232 be factored into a spatial part and an angular part. We assume that the thickness of
 233 the light sheet is approximately uniform over the field of view and that the detection-
 234 side point-response function is axially Gaussian over the width of the excitation light
 235 sheet, assumptions that we find to be true of our light sheets (further assumptions
 236 and details are provided in **Supplements 5.2–7**).

237 Our goal is to estimate the spatial distribution of ODFs, $f(\mathbf{r}_o, \hat{\mathbf{s}}_o)$, from the
 238 measured data, $g_{pv}(\mathbf{r}_d)$, but computing and inverting **Equation 1** is extremely com-
 239 putationally expensive. We reformulate **Equation 1** using *spatio-angular transfer*
 240 *functions* to simplify our computations and inversions with the additional benefit of
 241 improving our intuition about the imaging system’s limits (**Supplement 6**). We apply
 242 *spatial and spherical Fourier transforms* to exploit the symmetries and bandlimits of
 243 **Equation 1** to rewrite it as

$$G_{pv}(\mathbf{v}) = \sum_{\ell=0,2,4} \sum_{m=-\ell}^{\ell} H_{pv,\ell m}(\mathbf{v}) F_{\ell m}(\mathbf{v}) \quad \text{for } |\mathbf{v}_v^\perp| < 2NA_v/\lambda, \quad (2)$$

244 where $G_{pv}(\mathbf{v}) = \mathcal{F}_{\mathbb{R}^3}\{g_{pv}(\mathbf{r})\}$ is the *irradiance spectrum*, the 3D spatial Fourier
 245 transform of the measured irradiance; $H_{pv,\ell m}(\mathbf{v}) = \mathcal{F}_{\mathbb{R}^3 \times \mathbb{S}^2}\{h_{pv}(\mathbf{r}, \hat{\mathbf{s}}_o)\}$ is the *dipole*
 246 *spatio-angular transfer function*, the 3D spatial and spherical Fourier transform of
 247 the spatio-angular point response function; $F_{\ell m}(\mathbf{v}) = \mathcal{F}_{\mathbb{R}^3 \times \mathbb{S}^2}\{f(\mathbf{r}, \hat{\mathbf{s}}_o)\}$ is the sam-
 248 ple’s *dipole spatio-angular spectrum*; $\mathbf{v} \in \mathbb{R}^3$ is a three-dimensional spatial-frequency
 249 coordinate; $\mathbf{v}_v^\perp \in \mathbb{R}^2$ is a two-dimensional transverse spatial-frequency coordinate for
 250 each view; ℓ is the *spherical harmonic band index*, interpretable as the sharpness of an
 251 angular component; m is the *spherical harmonic intra-band index*, interpretable as the
 252 index over all orientation components at a specific angular sharpness ℓ ; $NA_A = 1.1$
 253 and $NA_B = 0.67$; and λ is the detection wavelength. The key features of **Equation**
 254 **2** are (1) *spatial band limits*: transverse spatial frequencies beyond $2NA/\lambda$ are not
 255 detected; (2) *angular discreteness*: instead of the continuous integral over the angular
 256 coordinate in **Equation 1** the transfer function formulation uses a discrete sum over
 257 spherical harmonic coefficients; and (3) *angular band limits*: angular frequencies from
 258 the $\ell = 0, 2$, and 4 bands are the only terms transmitted. **Figure 2(b)** demonstrates
 259 that an arbitrary ODF can be decomposed into a weighted sum of spherical harmon-
 260 ics, that a bandlimited version of an ODF is a smoother version of the original, and
 261 that missing intra-band components can distort an ODF.

262 With an efficient forward model (**Equation 2**) in hand, we used simulations
 263 (**Figure 2(c)(i, ii)**) to develop a Tikhonov-regularized least-squares reconstruction
 264 algorithm (**Figure 2(c)(iii, iv)**, **Supplements 7.1 and 7.2**). The spatio-angular
 265 coupling of the point-response function implies that we need to solve a small inverse
 266 problem for each spatial frequency—we cannot solve a small angular problem then
 267 solve a separate spatial problem. Therefore, our core algorithm consists of (1) applying
 268 a 3D spatial Fourier transform to the deskewed, registered, and calibrated volumes,
 269 (2) collecting the Fourier coefficients from each polarization and view into a 6×1
 270 vector, one vector for each spatial frequency, then (3) multiplying each vector by a
 271 precomputed spatial-frequency-specific 15×6 matrix before (4) applying an inverse

272 3D Fourier transform and storing the result: a set of 15 spherical harmonic coefficients
273 for each spatial point (**Supplement 7.3 and Supplement Table 4**).

274 We found that directly visualizing the complete reconstruction, a 3D spatial distri-
275 bution of ODFs (**Figure 2(c)(iv)**) provided the most information about the sample
276 but was visually overwhelming for most applications. We developed several tools for
277 reducing the visual complexity of the reconstructions (**Supplements 7.4 and 7.5**)
278 including peak-cylinder visualizations where the color and orientation of each cylinder
279 encodes the axis along which most dipoles are oriented (**Figure 2(c)(v)**), histogram
280 visualizations showing peak orientations in larger regions (**Figure 2(c)(vii)**), and
281 scalar metrics including density, proportional to the number of dipoles in each region
282 (**Figures 2(c)(vi, viii)**) and generalized fractional anisotropy (GFA) [33].

283 **2.3 Light-sheet tilting enables recovery of all** 284 **three-dimensional orientations**

285 The angular band limit of our transfer function (**Equation 2**) deserves additional
286 interpretation. Selective excitation with linearly polarized light will generate excited
287 ODFs of the form $\cos^2 \theta$ multiplied by the object ODF, which means that angu-
288 lar components of degree two, the $\ell = 2$ spherical harmonics, from the object ODF
289 can be encoded into detected irradiances. Similarly, selective detection will generate
290 irradiance patterns of the form $C_1 + C_2 \sin^2 \phi$ multiplied by the excited ODF (the
291 constants C_1 and C_2 are due to the finite detection numerical aperture), meaning
292 that selective excitation can encode the angular components of degree zero and two,
293 the $\ell = 0$ and $\ell = 2$ spherical harmonics. When we combine selective excitation and
294 detection, the imaging system can encode the $\ell = 0, 2$ and 4 components of the object
295 ODF into the measured irradiance patterns. Similar to spatial structured illumination
296 microscopy (SIM), angularly structured (polarized) illumination aliases high angular
297 frequency components into the detection pass band. Additionally, only even ℓ terms
298 are transmitted—antipodally symmetric ODFs mean that ODFs consist of only even- ℓ
299 terms.

300 This argument led us to expect that we could recover all orientations from our
301 sample by exploiting selective excitation and detection, using oversampled illumination
302 polarizations if necessary. We found our intuition to be incorrect, finding that no
303 number of illumination polarizations was enough to recover all orientations from our
304 imaging system. A close inspection of our angular transfer function revealed that we
305 did not properly consider *intra-band angular holes*.

306 **Figure 3(a)** shows all fifteen $\ell = 0, 2$ and 4 spherical harmonics along with the
307 four intra-band angular holes in our transfer function. Mathematically, the spherical
308 harmonic functions are grouped into $(2\ell + 1)$ -dimensional bands that form rotationally
309 invariant subspaces of the spherical functions, so if a single member of a band is
310 missing we cannot expect rotationally invariant angular resolution. The $\ell = 2$ and
311 $m = 1$ spherical harmonic, shown in **Figure 3(b)**, is a particularly consequential
312 angular hole because it is the single missing member of the lowest non-zero-order $\ell = 2$
313 band, implying that there are some orientations that we cannot recover. We can use
314 an abstract argument to predict this null function by inspection: all multiples of this
315 spherical harmonic are invisible to our imaging system because excitation/detection

316 of positive-valued lobes is always cancelled by excitation/detection of negative-valued
317 lobes.

318 We asked what a minimally modified version of our imaging system without an
319 $\ell = 2$ angular hole would look like, and we used the abstract argument above to propose
320 that *light-sheet tilting* (**Figure 3(c)**, **Supplement 2.2**, **Supplemental Figures S2**
321 **and S3**), enabled by a MEMS mirror placed conjugate to the illumination pupil,
322 would allow us to fill the angular hole in the transfer function while illuminating the
323 same spatial region.

324 We need to make at least 6 tilting polarization-diverse measurements to recover
325 components from all members of the $\ell = 0$ and 2 bands. We simulated transfer func-
326 tions and optimized the condition number of our sampling schemes, searching through
327 $\sim 2 \times 10^6$ possible sampling schemes to settle on the schemes depicted in **Figures**
328 **3(d, e)(i)**. **Supplements 2 and 8** provide more detail about our sampling choices.

329 Although we measure some components from the $\ell = 4$ band, we do not recover
330 all of its components. Our imaging system can access all orientations by recovering
331 components from all members of a non-zero band. Recovering the $\ell = 4$ band would
332 enable better angular resolution, but it would not enable access to more orientations
333 than the $\ell = 2$ band.

334 **Figures 3(d, e)** compare a peak-cylinder reconstruction of a GUV with and with-
335 out light-sheet tilting. The GUV is labelled with FM1-43, a membrane-crossing dye
336 with a dipole transition moment oriented normal to the membrane [34], so we expect
337 a pin-cushion-like reconstruction. **Figures 3(d)(ii, iv)** show incorrect peak cylinder
338 orientations in areas marked with red arrows—peak cylinders lie flat on the surface of
339 the GUV when they should point radially outward. **Figures 3(e)(ii, iv)** show that
340 light-sheet tilting corrects the problem, with continuously radial peak cylinders across
341 the surface of the GUV, highlighted in regions with green arrows. All subsequent data
342 and reconstructions are performed with light-sheet tilting.

343 2.4 pol-diSPIM measurements of fixed samples validate and 344 extend our knowledge of oriented biological structures

345 Having demonstrated that light-sheet tilting enables recovery of all orientations in
346 GUVs, we proceeded to validate and apply our method to other three-dimensional
347 samples (**Figure 4**, **Supplemental Movies M1–6**) including GUV, xylem, and
348 actin samples. **Figure 4(a)** shows ODF, peaks, density, and radial profile views of the
349 FM1-43-labelled GUV from **Figure 3**. While the peak-cylinder visualization (**Figure**
350 **4(a)(ii)**) is the easiest-to-interpret reconstruction, the ODF reconstruction can reveal
351 the subtlest changes that our system can measure, e.g. two different ODFs can have
352 identical peak cylinders. The density reconstruction (**Figure 4(a)(iii)**, **Supplemen-**
353 **tal Movies M1–2**) gives a view that is familiar to fluorescence microscopists, with
354 brightness encoding the density. Finally, we measure radial profiles (**Figure 4(a)(iv)**)
355 of the density (**Figure 4(b)(v)**) indicating that the fluorophores are most dense near
356 the GUV's surface with two-fold variation in intensity due to the non-uniform spatial
357 transfer function of our imaging system—although the transfer function is non-zero for
358 the second-order harmonics, it remains non-uniform. We also measure radial profiles
359 of the generalized fractional anisotropy (GFA) (**Figure 4(a)(vi)**) a scalar measure

360 with $GFA = 1$ indicating a strongly anisotropic structure and $GFA = 0$ indicating
361 an isotropic structure. The GFA profiles show similar behavior for all orientations,
362 starting at ~ 0.6 near the GUV's center, dipping to ~ 0.25 , then reaching peaks of
363 ~ 0.75 at the GUV's surface before dropping again. The behavior near the peak can
364 be interpreted as the increase in oriented structures compared to the random orienta-
365 tions nearby, but the high GFA value in the center of the GUV indicates the effects of
366 noise in low density regions. We consistently observed experiment-to-experiment vari-
367 ation in the value of GFA and orientations in background regions, leading us to only
368 draw conclusions from GFA and peaks in regions with a density above a background
369 threshold.

370 **Figure 4(b)** shows fast-scarlet labelled cellulose in a xylem cell (**Supplemental**
371 **Movies M3–4**), showing dipole orientations parallel to the long axis of the cellulose
372 fibers as expected from 2D studies [35]. We observe 3D orientations tracking the
373 cellulose fibers as they curve in space, spatially-disorganized orientation regions on
374 the basal surface near the cover slip, and the ability to distinguish cellulose fibers
375 that were indistinguishable on the basis of their merged density, but exhibited distinct
376 orientations (**Figure 4(b)(v)**). The disorganization on the basal side is consistent
377 with damage caused by air drying during sample preparation. The thinness of the
378 helices likely indicate a cell in the early stages of differentiation, which would make
379 these cells particularly susceptible to damage via air drying.

380 **Figure 4(c)** shows Alexa Fluor 488 phalloidin-labelled actin in a U2OS cell
381 (**Supplemental Movies M5–6**), showing dipole orientations parallel to the long axis
382 of the actin filaments as expected [22]. We observe distinct actin filaments, some lying
383 flat in the plane of the coverslip while others reach off the coverslip oriented nearly
384 normal to its surface.

385 2.5 pol-diSPIM measurements of cells grown on nanowires 386 show local-global alignment correlations

387 Having validated our system's ability to measure 3D orientations in actin, we used
388 our system to study actin orientations with respect to fixed landmarks by imag-
389 ing phalloidin-labelled 3T3 mouse fibroblasts grown on nanowire arrays (**Figures**
390 **5 and 6**), a model system for studying cell migration.

391 Cells' immediate environment, the extracellular matrix (ECM), is fibrous, consist-
392 ing of individual fibrils and bundled fibers ranging in diameter from a few hundred
393 nanometers to several micrometers [36–38], organized in a diverse range of fiber den-
394 sities, pore sizes, and network architectures, including aligned [39] and crossed-fiber
395 arrangements [40–43]. The complexity of studying cell migration in 3D motivated stud-
396 ies with simpler 1D substrates, which were found to replicate many of the features
397 of 3D matrices while differing from observations on conventional 2D culture systems
398 [44]. Further, in fibrous environments with large pore sizes, cells contact only a few
399 fibers, signifying that cells in vivo can be suspended [45–48] and that imaging cells
400 suspended on 1D and 2D wire arrays can provide biological insight.

401 Previously, we showed that cellular shapes can be tuned to the underlying fiber
402 network, with actin stress fibers aligning along ECM-fibers in cells attached to sin-
403 gle and multiple parallel fibers, and intersecting actin networks in cells attached to

404 a crosshatch network of fibers [49, 50]. In a subsequent study, the underlying actin
405 networks were found to regulate mitotic outcomes through actin retraction fibers con-
406 necting the rounded mitotic cell body to interphase adhesion sites [51]. In both studies,
407 while the patterning of actin networks matched the arrangement of underlying ECM
408 networks, it was unclear how far the effect of adhesions on fibers was extended to
409 shape the actin networks.

410 Here we used pol-diSPIM imaging to investigate long-range adhesion effects in 3D.
411 We deposited suspended fibers ~ 200 nm in diameter, imaged phalloidin-labelled 3T3
412 mouse fibroblasts grown on these nanowire arrays, and measured the local orientation
413 of actin networks. We imaged in two channels, a 488 nm channel for wire annotation,
414 and a 561 nm channel for orientation measurements (**Supplement 4.3**).

415 **Figure 5(a)** shows a density reconstruction of a single cell with ROIs highlighted
416 for closer inspection. The peak cylinders (**Figure 5(b)**) indicate that actin filaments
417 and the dipoles that label them coalign with their nearest nanowires, and the his-
418 tograms (**Figure 5(c)**) show distinct in-plane and out-of-plane filament populations
419 from within each ROI, including out-of-plane populations that would be invisible
420 to traditional anisotropy measurements. Additionally, we observe more disorder and
421 larger out-of-plane populations for ROIs near the center of the cell (**Figure 5(b-c)(ii,**
422 **iv)**) than regions near nanowires (**Figure 5(b-c)(i, (iii), (v)**).

423 To evaluate dipole orientations of F-actin with respect to their nearest wires, we
424 developed a pair of scalar metrics, parallelism and radially (**Supplement 7.6**), and
425 computed maps of these metrics in regions with a total number of counts across
426 polarizations and views greater than 5000, a threshold that rejects background regions.

427 We used these metrics to further investigate nine FOVs, with three FOVs for
428 each of three different nanowire arrangements: single, paired, and crossed nanowires
429 (**Figure 6(a)**). Across each FOV we calculated parallelism and radially for voxels
430 $< 5 \mu\text{m}$ from their nearest wire, and we compared these metrics between FOVs and
431 wire arrangements (**Figure 6(b)**). We found the FOVs with the same wire arrange-
432 ment clustered at distinct parallelism and radially values and showed no significant
433 differences (colors in **Figure 6(c)**), while FOVs with different wire arrangement
434 showed significantly different values for parallelism and radially. The crossed wire
435 arrangement showed significantly lower parallelism (0.70 ± 0.24 , mean \pm standard
436 deviation across voxels) than single (0.88 ± 0.11) and paired (0.89 ± 0.11) arrange-
437 ments, indicating local-scale disorder of actin filaments created by the presence of
438 wires in multiple orientations. Consistent with this observation, cells on crossed wires
439 showed significantly increased radially (0.51 ± 0.28) over cells on single wires (0.17
440 ± 0.13). **Figure 5(v)** shows an ROI consistent with these broader conclusions, where
441 peaks show increased disorder near a wire crossing.

442 Further, we calculated each FOV's aspect ratio, a global measure of the effect of
443 nanowire topology on cell polarization, and found that the aspect ratio was positively
444 and negatively correlated with parallelism ($r = 0.66$) and radially ($r = -0.78$),
445 respectively. Both of these correlations are interpretable as evidence for local-global
446 coordination in the architecture of these cells as they grow on their extra-cellular
447 matrix substrates.

448 Taken together, our measurements demonstrate, for the first time to our knowl-
449 edge, that the effect of parallel ECM networks in orienting actin is felt over cell-scale
450 distances, and topographical intersections diminish the orientation. Our findings are
451 consistent with previous studies of 2D actin filament orientation and cell shape [52],
452 and we are excited by our system's ability to extend these findings to 3D.

453 3 Discussion

454 This work develops a theoretical and experimental bridge between 2D anisotropy
455 measurements and 3D single-molecule orientation measurements. ODFs and the
456 spatio-angular transfer function formalism helped us identify the limits of our imaging
457 system, and we used theory to improve our design with light-sheet tilting. A similar
458 light-sheet tilting scheme was used to reduce absorptive-streaking artefacts [53], but
459 here we use tilting to increase the angular diversity of polarized illumination, allow-
460 ing us to recover all orientations to extend and draw new conclusions about oriented
461 fluorescent samples in 3D.

462 Spatio-angular transfer functions point us towards further improvements. Designs
463 that use polarization splitting to make simultaneous selective-detection measurements
464 will give access to the $\ell = 4$ band without trading off speed, and designs that have
465 a more uniform angular response than our system will improve on our ability to
466 draw conclusions from samples in all orientations. Polarized two-photon excitation and
467 emission [54] provide $\cos^4 \theta$ -behavior, sharper than the single-photon $\cos^2 \theta$ -behavior
468 considered here, leading to potential for accessing the $\ell = 6$ and 8 bands.

469 Imaging speed limits our ability to draw conclusions from living cells. We measure
470 orientation signals via serial polarized illumination measurements taken over a few
471 seconds, so translational motion on this timescale is indistinguishable from an oriented
472 sample. Although we made many measurements of living cells with our system, we
473 decided to withhold these data from publication as the possibility of spatial motion
474 repeatedly called our conclusions into question. Replacing our polarized illumination
475 strategy with a detection-side polarization splitting strategy provides one path for
476 speed improvement.

477 We were constrained by a limited palette of fluorescent reporters that rigidly attach
478 to biological structures. Although we are encouraged by recent developments of genet-
479 ically encoded actin orientation probes [55], we see room for development of bright
480 oriented probes across the spectrum in more biological structures. We see probes as
481 the major limitation in this field, not instrumentation.

482 Here we made steady-state measurements, considering only quasi-static fluorescent
483 reporters. Time-resolved orientation measurements provide a large set of possibili-
484 ties for this field [56, 57], and combining time-resolved measurements with reversibly
485 switchable proteins allows measurement of a wide range of reorientation timescales
486 [58], giving access to reorientation timescales of large protein complexes. We are
487 excited for future developments that probe long-timescale reorientation of fluorophores
488 trapped in 3D angular potentials.

489 Fluorescence anisotropy can be used for homoFRET measurements of molecular
490 binding [59], and an early non-tilting variant of the system described here was used

491 to make such measurements [60]. We hope that future efforts will encode additional
492 physical parameters, such as force and voltage, into the orientation and rotational
493 mobility of fluorescent probes with readouts enabled by systems like the one described
494 here.

495 **4 Online Methods**

496 This section describes all sample-preparation protocols. All imaging and analysis
497 details can be found in the supplementary materials.

498 **4.1 Bead samples**

499 Glass coverslips (24 mm × 60 mm, #1.5, Electron Microscopy Sciences, 63793-01)
500 were cleaned with clean water and coated with 0.1% poly(l-lysine) (Sigma-Aldrich,
501 P8920) for 10 minutes. 100 nm diameter yellow-green beads (Thermo Fisher Scientific,
502 F8803) were diluted $\sim 10^5$ -fold, and 20 μL added to the coverslip. After 10 minutes,
503 the coverslip was washed three times with clean water before imaging. Beads were
504 used to obtain measured estimates of the system PSF, which in turn were used to
505 guide the generation of theoretical PSFs.

506 **4.2 Fluorescence slides**

507 For system calibration, a fluorescent plastic slide (Chroma, 92001) was carefully cut
508 into small pieces ($\sim 4 \times 5 \text{ mm}^2$) and glued to a glass coverslip (24 mm × 60 mm,
509 #1.5, Electron Microscopy Sciences, 63793-01). Then the coverslip was mounted to a
510 chamber (Applied Scientific Instrumentation, I-3078-2460) and imaged with diSPIM
511 objectives to measure fluorescence changes as we varied the excitation modulation.

512 **4.3 Giant unilamellar vesicles samples**

513 We prepared giant unilamellar vesicles (GUVs) via electroformation [61, 62]. We coated
514 a coverslip with 20 μL cBSA, waited for ~ 15 minutes at room temperature for it to
515 dry into a thin layer, then washed three times with distilled water. We mixed 2 μL
516 of FM1-43 (ThermoFisher, a membrane-crossing dye with a dipole transition moment
517 oriented normal to the membrane [63]) and 40 μL of GUV solution in a 1.5 mL tube,
518 transferred the solution to the cBSA coated coverslip, and waited for ~ 20 minutes
519 for GUVs to settle. Finally, we placed the coverslip in the imaging chamber, filled
520 it with sucrose solution, and waited ~ 12 hours, covered with a thin film to reduce
521 evaporation, before imaging.

522 **4.4 Fixed plant xylem samples**

523 Xylem cells were prepared by inducing tobacco (*Nicotiana tabacum*) BY-2 cells to
524 differentiate into tracheary elements, as described by Yamaguchi et al. [64]. Briefly,
525 cells were cultured with standard methods for BY-2 [65]. A stable cell line was gen-
526 erated in which a transcription factor (VND7), driven by an inducible promoter
527 (dexamethasone), had been integrated into the genome. Four days after adding 1 μM

528 dexamethasone to the culture, cells were collected, stained for 30 minutes with 0.02%
529 fast scarlet in growth medium, rinsed in growth medium, adhered to poly-L-lysine
530 coated coverslips, and air dried. Fast scarlet binds cellulose in an oriented manner [66].

531 4.5 Fixed U2OS cells with labelled actin

532 U2OS cells (American Type Culture Collection, HTB-96) were cultured in DMEM
533 media (Lonza, 12-604F) supplemented with 10% FBS (Thermo Fisher Scientific,
534 A4766801) at 37°C and 5% CO₂ on coverslips. Cells were fixed by 2% paraformalde-
535 hyde (Electron Microscopy Sciences, 15711) in 1× PBS at room temperature for 15
536 minutes and rinsed three times with 1× PBS. Cells were incubated with Alexa Fluor
537 488 phalloidin (Invitrogen, A12379, 1:50 dilution in 1× PBS) for 1 hour at room
538 temperature and rinsed three times with 1× PBS before imaging.

539 4.6 Fiber network manufacturing

540 Polystyrene fibers were manufactured using the non-electrospinning spinneret-based
541 tunable engineered parameters (STEP) platform as previously reported [67, 68].
542 Polystyrene of two different molecular weights (Agilent, $M_w = 15 \times 10^6$ g/mol and
543 Polystyrene Standard, $M_w = 2.5 \times 10^6$ g/mol) was dissolved in xylene (Carolina Chem-
544 icals) to form polymeric solutions at 5% (w/w). Additionally, 20 μ L of 1 mg/mL of
545 BDP FL Maleimide dye (Lumiprobe) was added to the polymer solutions to get flu-
546 orescent fibers. Fibers were spun on hollow 5 × 5 mm metal scaffolds. The first layer
547 of fibers deposited were large diameter fibers $\sim 2 \mu$ m ($M_w = 15 \times 10^6$ g/mol) fol-
548 lowed by an orthogonal layer of 200 nm ($M_w = 2.5 \times 10^6$ g/mol) fibers with spacing
549 varying from 7 to 20 μ m to achieve a variety of cell shapes (elongated on single fibers
550 and parallel-shaped cells on two or more fibers) [51, 69, 70]. Additionally, crosshatch
551 networks of 200 nm fiber diameters were also prepared with spacing varying from 7
552 to 20 μ m [50, 71] to achieve polygonal and kite-shaped cells on multiple fibers. The
553 fiber networks were fused at junctions using a custom-built chemical fusing chamber.

554 4.7 Cell culture and seeding on fiber networks

555 3T3 mouse fibroblasts (ATCC) were grown in Dulbecco's modified Eagle's medium
556 (Corning) supplemented with 10% fetal bovine serum (Corning) in T25 flasks (Thermo
557 Scientific). The cells were grown in an incubator kept at 37°C and 5% CO₂. The
558 nanofiber network scaffolds were tacked on a cover glass (VWR, 24 × 60 mm No. 1.5)
559 with the help of high-vacuum grease (Dow Corning). Next, the scaffolds were steril-
560 ized with 70% ethanol for 10 minutes followed by Phosphate Buffer Solution (PBS)
561 washes (two times). Next, the scaffold was coated with 4 μ g/mL bovine fibronectin
562 (Sigma Aldrich) in PBS for at least one hour to promote cell adhesion. Cells were
563 then seeded onto the scaffolds with a seeding density of 300,000 cells/mL and were
564 allowed to spread onto the fibers for a few hours followed by the addition of 3 mL of
565 media. Cells were allowed to further spread for an additional 24 hours before fixation.

566

567 4.8 Immunostaining cells on fiber networks

568 Cells were fixed with 4% paraformaldehyde in PBS (Santa Cruz Chemicals) for 15 min-
569 utes. The cells were then washed with PBS two times and then permeabilized with
570 0.1% Triton X-100 solution. Following two PBS washes the cells were blocked with 5%
571 goat serum (Fisher Scientific) for 30 minutes. Next, conjugated antibody Alexa Fluor
572 568 Phalloidin (1:100, Thermo Fisher) diluted in antibody dilution buffer was added
573 to the cells. After one hour, the cells were washed with PBS (3×, 5 minutes each).
574 The sample was then covered in 2 mL of Live Cell Imaging Media (Thermo Fisher)
575 for imaging.

576 **Acknowledgements.** We thank Applied Scientific Instrumentation (ASI) for shar-
577 ing drawings and assisting with hardware.

578 **Supplementary information.** This manuscript is accompanied by a supplemen-
579 tary document with 9 text supplements, 4 tables, 13 figures, and 6 movies.

580 **Funding.** This research was supported by the intramural research programs of the
581 National Institute of Biomedical Imaging and Bioengineering, National Institutes of
582 Health. We thank the Marine Biological Laboratories (MBL), for providing a meet-
583 ing and brainstorming platform. T. C. was supported by a University of Chicago
584 Biological Sciences Division Graduate Fellowship and an O'Brien–Hasten Research
585 Collaboration Award. H. S. and P. L. R. acknowledge the Whitman Fellows program
586 at MBL for providing funding and space for discussions valuable to this work. P. L.
587 R. acknowledges funding from the NIH under grant no. R01EB026300. This research
588 is funded in part by the Gordon and Betty Moore Foundation. This work was sup-
589 ported by the Howard Hughes Medical Institute (HHMI) and the Janelia Visiting
590 Scientists Program. This article is subject to HHMI's Open Access to Publications
591 policy. HHMI lab heads have previously granted a nonexclusive CC BY 4.0 license to
592 the public and a sublicensable license to HHMI in their research articles. Pursuant to
593 those licenses, the author-accepted manuscript of this article can be made freely avail-
594 able under a CC BY 4.0 license immediately upon publication. A. K. would like to
595 acknowledge funding from the CZI through Imaging Scientist Program and the Arnold
596 and Mabel Beckman Foundation for the lightsheet award. Work in the Baskin labo-
597 ratory on cellulose is supported by the Division of Chemical Sciences, Geosciences,
598 and Biosciences, Office of Basic Energy Sciences of the U.S. Department of Energy
599 under grant no. DE–FG–03ER15421. R. O. gratefully acknowledges funding from the
600 NIH/NIGMS under grant no. R35GM131843 and from the Marine Biological Labora-
601 tory through the Inoué Endowment Fund. This material is based upon work supported
602 by the National Science Foundation under grant no. 2119949 and grant no. 2107332.

603 **Conflict of interest/Competing interests.** H. S., A. K., S. M., P. L. R., R. O.,
604 Y. W., and T. C. hold US Patent # 11428632.

605 **Ethics approval and consent to participate.** Not applicable.

606 **Consent for publication.** Not applicable.

607 **Data availability.** Registered data, analysis scripts, reconstructions, and visual-
608 izations of all samples described here are available on the BioImage Archive at
609 <https://www.ebi.ac.uk/biostudies/bioimages/studies/S-BIAD1055>.

610 **Materials availability.** Not applicable.

611 **Code availability.** Pre-processing analysis software is available at <https://github.com/eguomin/microImageLib>. Reconstruction and visualization software is
612 available at <https://github.com/talonchandler/polaris>. Several visuals were enabled
613 by Dipy [72].
614

615
616 **Author contributions.** T. C. developed theory, analysis, and visualization
617 tools; suggested theory-motivated experimental improvements; performed all post-
618 registration analysis; and drafted the paper, figures, and supplements. M. G. built
619 the microscope, aligned and calibrated its optical system, modified its hardware and
620 software to support light-sheet tilting, acquired all data, and performed all data pre-
621 processing. Y. S., J. C., and V. J. prepared cellular samples. J. L. and H. L. contributed
622 to analysis pipelines. Y. W. contributed to preprocessing software and an early pro-
623 totype system. A. A. prepared and interpreted nanowire samples. S. B. M. and A. K.
624 contributed to an early prototype of the microscope. T. B. prepared and interpreted
625 xylem samples. R. F., A. N., and V. S. contributed biological context, guided our
626 nanowire investigations, and interpreted nanowire and live-cell samples. R. O. prepared
627 GUV samples and provided experimental, theoretical, and interpretation guidance.
628 P. L. R. and H. S. oversaw the work, contributing to theory, experiment, analysis,
629 visualization, interpretation, and writing. All coauthors contributed to revisions.

630 References

- 631 [1] Brasselet, S., Alonso, M.A.: Polarization microscopy: from ensemble structural
632 imaging to single-molecule 3D orientation and localization microscopy. *Optica*
633 **10**(11), 1486–1510 (2023) <https://doi.org/10.1364/OPTICA.502119>
- 634 [2] Lakowicz, J.R.: Principles of Fluorescence Spectroscopy, 3rd edn. Springer, New
635 York (2006)
- 636 [3] Jameson, D.M., Ross, J.A.: Fluorescence polarization/anisotropy in diagnostics
637 and imaging. *Chemical Reviews* **110**(5), 2685–2708 (2010) [https://doi.org/10.](https://doi.org/10.1021/cr900267p)
638 [1021/cr900267p](https://doi.org/10.1021/cr900267p)
- 639 [4] Axelrod, D.: Carbocyanine dye orientation in red cell membrane studied by
640 microscopic fluorescence polarization. *Biophysical Journal* **26**(3), 557–573 (1979)
641 [https://doi.org/10.1016/S0006-3495\(79\)85271-6](https://doi.org/10.1016/S0006-3495(79)85271-6)
- 642 [5] Ferrand, P., Gasecka, P., Kress, A., Wang, X., Bioud, F.-Z., Duboisset, J.,
643 Brasselet, S.: Ultimate use of two-photon fluorescence microscopy to map orien-
644 tational behavior of fluorophores. *Biophysical Journal* **106**(11), 2330–2339 (2014)
645 <https://doi.org/10.1016/j.bpj.2014.04.011>

- 646 [6] Vrabioiu, A.M., Mitchison, T.J.: Structural insights into yeast septin organization
647 from polarized fluorescence microscopy. *Nature* **443**(7110), 466–469 (2006) <https://doi.org/10.1038/nature05109>
648
- 649 [7] DeMay, B.S., Noda, N., Gladfelter, A.S., Oldenbourg, R.: Rapid and quantitative
650 imaging of excitation polarized fluorescence reveals ordered septin dynamics in
651 live yeast. *Biophysical Journal* **101**(4), 985–994 (2011) [https://doi.org/10.1016/](https://doi.org/10.1016/j.bpj.2011.07.008)
652 [j.bpj.2011.07.008](https://doi.org/10.1016/j.bpj.2011.07.008)
- 653 [8] McQuilken, M., Jentzsch, M.S., Verma, A., Mehta, S.B., Oldenbourg, R., Glad-
654 felter, A.S.: Analysis of septin reorganization at cytokinesis using polarized
655 fluorescence microscopy. *Frontiers in Cell and Developmental Biology* **5**(42)
656 (2017) <https://doi.org/10.3389/fcell.2017.00042>
- 657 [9] Kampmann, M., Atkinson, C.E., Mattheyses, A.L., Simon, S.M.: Mapping the
658 orientation of nuclear pore proteins in living cells with polarized fluorescence
659 microscopy. *Nature Structural and Molecular Biology* **18**(6), 643–649 (2011)
660 <https://doi.org/10.1038/nsmb.2056>
- 661 [10] Brockman, J.M., Blanchard, A.T., Pui-Yan Ma, V., Derricotte, W.D., Zhang, Y.,
662 Fay, M.E., Lam, W.A., Evangelista, F.A., Mattheyses, A.L., Salaita, K.: Mapping
663 the 3D orientation of piconewton integrin traction forces. *Nature Methods* **15**,
664 115–118 (2017) <https://doi.org/10.1038/nmeth.4536>
- 665 [11] Blanchard, A.T., Brockman, J., Salaita, K., Mattheyses, A.L.: Variable incidence
666 angle linear dichroism (VALiD): A technique for unique 3D orientation mea-
667 surement of fluorescent ensembles. *Optics Express* **28**(7), 10039–10061 (2020)
668 <https://doi.org/10.1364/OE.381676>
- 669 [12] Smalyukh, I.I., Shiyonovskii, S.V., Lavrentovich, O.D.: Three-dimensional imag-
670 ing of orientational order by fluorescence confocal polarizing microscopy. *Chemical*
671 *Physics Letters* **336**(1), 88–96 (2001) [https://doi.org/10.1016/S0009-2614\(00\)](https://doi.org/10.1016/S0009-2614(00)01471-8)
672 [01471-8](https://doi.org/10.1016/S0009-2614(00)01471-8)
- 673 [13] Ohzono, T., Katoh, K., Fukuda, J.: Fluorescence microscopy reveals molecular
674 localisation at line defects in nematic liquid crystals. *Scientific Reports* **6**(36477),
675 1–9 (2016) <https://doi.org/10.1038/srep36477>
- 676 [14] Zhanghao, K., Chen, X., Liu, W., Li, M., Liu, Y., Wang, Y., Luo, S., Wang,
677 X., Shan, C., Xie, H., Gao, J., Chen, X., Jin, D., Li, X., Zhang, Y., Dai, Q.,
678 Xi, P.: Super-resolution imaging of fluorescent dipoles via polarized structured
679 illumination microscopy. *Nature Communications* **10**(4694), 1–10 (2019) <https://doi.org/10.1038/s41467-019-12681-w>
680
- 681 [15] Guan, M., Wang, M., Zhanghao, K., Zhang, X., Li, M., Liu, W., Niu, J., Yang,
682 X., Chen, L., Jing, Z., Zhang, M.Q., Jin, D., Xi, P., Gao, J.: Polarization mod-
683 ulation with optical lock-in detection reveals universal fluorescence anisotropy

- 684 of subcellular structures in live cells. *Light: Science & Applications* **11**(4), 1–13
685 ([2022](https://doi.org/10.1038/s41377-021-00689-1)) <https://doi.org/10.1038/s41377-021-00689-1>
- 686 [16] Zhong, S., Qiao, L., Ge, X., Xu, X., Fu, Y., Gao, S., Zhanghao, K., Hao, H.,
687 Wang, W., Li, M., Xi, P.: Three-dimensional dipole orientation mapping with
688 high temporal-spatial resolution using polarization modulation. *bioRxiv* (2023)
689 <https://doi.org/10.1101/2023.12.12.571225>
- 690 [17] Wu, T., King, M.R., Farag, M., Pappu, R.V., Lew, M.D.: Mapping inhomogeneous
691 network structures within biomolecular condensate using single-molecule imaging
692 and tracking of fluorogenic probes. *Biophysical Journal* **122**(3), 296 (2023) <https://doi.org/10.1016/j.bpj.2022.11.1673>
- 694 [18] Backer, A.S., Biebricher, A.S., King, G.A., Wuite, G.J.L., Heller, I., Peterman,
695 E.J.G.: Single-molecule polarization microscopy of DNA intercalators sheds light
696 on the structure of S-DNA. *Science Advances* **5**(3) (2019) <https://doi.org/10.1126/sciadv.aav1083>
- 698 [19] Ding, T., Wu, T., Mazidi, H., Mazidi, H., Zhang, O., Lew, M.D.: Single-
699 molecule orientation localization microscopy for resolving structural hetero-
700 geneities between amyloid fibrils. *Optica* **7**(6), 602–607 (2020) <https://doi.org/10.1364/OPTICA.388157>
- 702 [20] Beausang, J.F., Shroder, D.Y., Nelson, P.C., Goldman, Y.E.: Tilting and wobble
703 of myosin V by high-speed single-molecule polarized fluorescence microscopy. *Bio-*
704 *physical Journal* **104**(6), 1263–1273 (2013) <https://doi.org/10.1016/j.bpj.2013.01.057>
- 706 [21] Zhang, O., Guo, Z., He, Y., Wu, T., Vahey, M.D., Lew, M.D.: Six-dimensional
707 single-molecule imaging with isotropic resolution using a multi-view reflector
708 microscope. *Nature Photonics* **17**(2), 179–186 (2023) <https://doi.org/10.1038/s41566-022-01116-6>
- 710 [22] Mehta, S.B., McQuilken, M., La Rivière, P.J., Occhipinti, P., Verma, A., Olden-
711 bourg, R., Gladfelter, A.S., Tani, T.: Dissection of molecular assembly dynamics
712 by tracking orientation and position of single molecules in live cells. *Proceedings*
713 *of the National Academy of Sciences of the United States of America* **113**(42),
714 6352–6361 (2016) <https://doi.org/10.1073/pnas.1607674113>
- 715 [23] Swaminathan, V., Kalappurakkal, J.M., Mehta, S.B., Nordenfelt, P., Moore, T.I.,
716 Koga, N., Baker, D.A., Oldenbourg, R., Tani, T., Mayor, S., Springer, T.A.,
717 Waterman, C.M.: Actin retrograde flow actively aligns and orients ligand-engaged
718 integrins in focal adhesions. *Proceedings of the National Academy of Sciences of*
719 *the United States of America* **114**(40), 10648–10653 (2017) <https://doi.org/10.1073/pnas.1701136114>
- 721 [24] Wu, Y., Wawrzusin, P., Senseney, J., Fischer, R.S., Christensen, R., Santella,

- 722 A., York, A.G., Winter, P.W., Waterman, C.M., Bao, Z., Colón-Ramos, D.A.,
723 McAuliffe, M., Shroff, H.: Spatially isotropic four-dimensional imaging with dual-
724 view plane illumination microscopy. *Nature Biotechnology* **31**(11), 1032–1038
725 (2013) <https://doi.org/10.1038/nbt.2713>
- 726 [25] Chandler, T., Mehta, S., Shroff, H., Oldenbourg, R., La Rivière, P.J.: Single-
727 fluorophore orientation determination with multiview polarized illumination:
728 Modeling and microscope design. *Optics Express* **25**(25), 31309–31325 (2017)
729 <https://doi.org/10.1364/OE.25.031309>
- 730 [26] Basser, P.J., Mattiello, J., Le Bihan, D.: MR diffusion tensor spectroscopy and
731 imaging. *Biophysical Journal* **66**(1), 259–267 (1994) [https://doi.org/10.1016/
732 S0006-3495\(94\)80775-1](https://doi.org/10.1016/S0006-3495(94)80775-1)
- 733 [27] Tuch, D.S.: Q-ball imaging. *Magnetic Resonance in Medicine* **52**(6), 1358–1372
734 (2004) <https://doi.org/10.1002/mrm.20279>
- 735 [28] Chandler, T., Shroff, H., Oldenbourg, R., La Rivière, P.J.: Spatio-angular fluo-
736 rescence microscopy I. Basic theory. *Journal of the Optical Society of America A*
737 **36**(8), 1334–1345 (2019) <https://doi.org/10.1364/JOSAA.36.001334>
- 738 [29] Chandler, T., Shroff, H., Oldenbourg, R., La Rivière, P.J.: Spatio-angular fluo-
739 rescence microscopy II. Paraxial $4f$ imaging. *Journal of the Optical Society of*
740 *America A* **36**(8), 1346–1360 (2019) <https://doi.org/10.1364/JOSAA.36.001346>
- 741 [30] Chandler, T., Shroff, H., Oldenbourg, R., La Rivière, P.J.: Spatio-angular fluo-
742 rescence microscopy III. Constrained angular diffusion, polarized excitation, and
743 high-NA imaging. *Journal of the Optical Society of America A* **37**(9), 1465–1479
744 (2020) <https://doi.org/10.1364/JOSAA.389217>
- 745 [31] Myšková, J., Rybakova, O., Brynda, J., Khoroshyy, P., Bondar, A., Lazar, J.:
746 Directionality of light absorption and emission in representative fluorescent pro-
747 teins. *Proceedings of the National Academy of Sciences of the United States of*
748 *America* **117**(51), 32395–32401 (2020) <https://doi.org/10.1073/pnas.2017379117>
- 749 [32] Wu, Y., Kumar, A., Smith, C., Ardiel, E., Chandris, P., Christensen, R., Rey-
750 Suarez, I., Guo, M., Vishwasrao, H.D., Chen, J., Tang, J., Upadhyaya, A.,
751 La Rivière, P.J., Shroff, H.: Reflective imaging improves spatiotemporal resolu-
752 tion and collection efficiency in light sheet microscopy. *Nature Communications*
753 **8**(1), 1452 (2017) <https://doi.org/10.1038/s41467-017-01250-8>
- 754 [33] Cheng, J., Basser, P.J.: Director field analysis (DFA): Exploring local white mat-
755 ter geometric structure in diffusion MRI. *Medical Image Analysis* **43**, 112–128
756 (2018) <https://doi.org/10.1016/j.media.2017.10.003>
- 757 [34] Abrahamsson, S., McQuilken, M., Mehta, S.B., Verma, A., Larsch, J., Ilic, R.,
758 Heintzmann, R., Bargmann, C.I., Gladfelter, A.S., Oldenbourg, R.: Multifocus

- 759 polarization microscope (MF-Polscope) for 3D polarization imaging of up to 25
760 focal planes simultaneously. *Optics Express* **23**(6), 7734–7754 (2015) <https://doi.org/10.1364/OE.23.007734>
761
- 762 [35] Thomas, J., Idris, N.A., Collings, D.A.: Pontamine fast scarlet 4B bifluorescence
763 and measurements of cellulose microfibril angles. *Journal of Microscopy* **268**(1),
764 13–27 (2017) <https://doi.org/10.1111/jmi.12582>
- 765 [36] Ushiki, T.: Collagen fibers, reticular fibers and elastic fibers. A comprehen-
766 sive understanding from a morphological viewpoint. *Archives of Histology and*
767 *Cytology* **65**(2), 109–126 (2002) <https://doi.org/10.1679/aohc.65.109>
- 768 [37] Fernández, M., Keyriläinen, J., Serimaa, R., Torkkeli, M., Karjalainen-Lindsberg,
769 M.-L., Tenhunen, M., Thomlinson, W., Urban, V., Suortti, P.: Small-angle x-
770 ray scattering studies of human breast tissue samples. *Physics in Medicine and*
771 *Biology*. **47**(4), 577 (2002) <https://doi.org/10.1088/0031-9155/47/4/303>
- 772 [38] Doyle, A.D., Carvajal, N., Jin, A., Matsumoto, K., Yamada, K.M.: Local
773 3D matrix microenvironment regulates cell migration through spatiotemporal
774 dynamics of contractility-dependent adhesions. *Nature Communications* **6**(8720),
775 1–15 (2015) <https://doi.org/10.1038/ncomms9720>
- 776 [39] Conklin, M.W., Eickhoff, J.C., Riching, K.M., Pehlke, C.A., Eliceiri, K.W.,
777 Provenzano, P.P., Friedl, A., Keely, P.J.: Aligned collagen is a prognostic signa-
778 ture for survival in human breast carcinoma. *The American Journal of Pathology*.
779 **178**(3), 1221–1232 (2011) <https://doi.org/10.1016/j.ajpath.2010.11.076>
- 780 [40] Weigelin, B., Bakker, G.-J., Friedl, P.: Intravital third harmonic generation
781 microscopy of collective melanoma cell invasion: Principles of interface guidance
782 and microvesicle dynamics. *Intravital* **1**(1), 32–43 (2012) <https://doi.org/10.4161/intv.21223>
783
- 784 [41] Clark, A.G., Vignjevic, D.M.: Modes of cancer cell invasion and the role of the
785 microenvironment. *Current Opinion in Cell Biology* **36**, 13–22 (2015) <https://doi.org/10.1016/j.ceb.2015.06.004>
786
- 787 [42] Glentis, A., Oertle, P., Mariani, P., Chikina, A., El Marjou, F., Attieh, Y.,
788 Zaccarini, F., Lae, M., Loew, D., Dingli, F., Sirven, P., Schoumacher, M.,
789 Gurchenkov, B.G., Plodinec, M., Vignjevic, D.M.: Cancer-associated fibroblasts
790 induce metalloprotease-independent cancer cell invasion of the basement mem-
791 brane. *Nature Communications* **8**(924), 1–13 (2017) <https://doi.org/10.1038/s41467-017-00985-8>
792
- 793 [43] Taylor, E.N., Hoffman, M.P., Aninwene 2nd, G.E., Gilbert, R.J.: Patterns of
794 intersecting fiber arrays revealed in whole muscle with generalized Q-space imag-
795 ing. *Biophysical Journal* **108**(11), 2740–2749 (2015) <https://doi.org/10.1016/j.bpj.2015.03.061>
796

- 797 [44] Doyle, A.D., Wang, F.W., Matsumoto, K., Yamada, K.M.: One-dimensional
798 topography underlies three-dimensional fibrillar cell migration. *Journal of Cell*
799 *Biology* **184**(4), 481–490 (2009) <https://doi.org/10.1083/jcb.200810041>
- 800 [45] Carey, S.P., Kraning-Rush, C.M., Williams, R.M., Reinhart-King, C.A.: Biophys-
801 ical control of invasive tumor cell behavior by extracellular matrix microarchi-
802 tecture. *Biomaterials* **33**(16), 4157 (2012) [https://doi.org/10.1016/j.biomaterials.](https://doi.org/10.1016/j.biomaterials.2012.02.029)
803 [2012.02.029](https://doi.org/10.1016/j.biomaterials.2012.02.029)
- 804 [46] Harley, B.A.C., Kim, H.-D., Zaman, M.H., Yannas, I.V., Lauffenburger, D.A.,
805 Gibson, L.J.: Microarchitecture of three-dimensional scaffolds influences cell
806 migration behavior via junction interactions. *Biophysical Journal* **95**(8), 4013–
807 4024 (2008) <https://doi.org/10.1529/biophysj.107.122598>
- 808 [47] Durgam, S., Singh, B., Cole, S.L., Brokken, M.T., Stewart, M.: Quantitative
809 assessment of tendon hierarchical structure by combined second harmonic gener-
810 ation and immunofluorescence microscopy. *Tissue Engineering Part C: Methods*
811 **26**(5), 253–262 (2020) <https://doi.org/10.1089/ten.TEC.2020.0032>
- 812 [48] Friedl, P., Wolf, K.: Plasticity of cell migration: a multiscale tuning model. *Journal*
813 *of Cell Biology* **188**(1), 11–19 (2010) <https://doi.org/10.1083/jcb.200909003>
- 814 [49] Sheets, K., Wunsch, S., Ng, C., Nain, A.S.: Shape-dependent cell migration
815 and focal adhesion organization on suspended and aligned nanofiber scaffolds.
816 *Acta Biomaterials* **9**(7), 7169–7177 (2013) [https://doi.org/10.1016/j.actbio.2013.](https://doi.org/10.1016/j.actbio.2013.03.042)
817 [03.042](https://doi.org/10.1016/j.actbio.2013.03.042)
- 818 [50] Jana, A., Nookaew, I., Singh, J., Behkam, B., Franco, A.T., Nain, A.S.: Crosshatch
819 nanofiber networks of tunable interfiber spacing induce plasticity in cell migration
820 and cytoskeletal response. *The FASEB Journal* **33**(10), 10618–10632 (2019) <https://doi.org/10.1096/fj.201900131R>
- 822 [51] Jana, A., Sarkar, A., Zhang, H., Agashe, A., Wang, J., Paul, R., Gov, N.S.,
823 DeLuca, J.G., Nain, A.S.: Mitotic outcomes and errors in fibrous environments.
824 *Proceedings of the National Academy of Sciences of the United States of America*
825 **120**(10), 2120536120 (2023) <https://doi.org/10.1073/pnas.2120536120>
- 826 [52] Schakenraad, K., Ernst, J., Pomp, W., Danen, E.H.J., Merks, R.M.H., Schmidt,
827 T., Giomi, L.: Mechanical interplay between cell shape and actin cytoskele-
828 ton organization. *Soft Matter* **16**(27), 6328–6343 (2020) [https://doi.org/10.1039/](https://doi.org/10.1039/D0SM00492H)
829 [D0SM00492H](https://doi.org/10.1039/D0SM00492H)
- 830 [53] Huisken, J., Stainier, D.Y.R.: Even fluorescence excitation by multidirectional
831 selective plane illumination microscopy (mspim). *Optics Letters* **32**(17), 2608–
832 2610 (2007) <https://doi.org/10.1364/OL.32.002608>
- 833 [54] Lazar, J., Bondar, A., Timr, S., Firestein, S.J.: Two-photon polarization

- 834 microscopy reveals protein structure and function. *Nature Methods* **8**(8), 684–690
835 (2011) <https://doi.org/10.1038/nmeth.1643>
- 836 [55] Nakai, N., Sato, K., Tani, T., Saito, K., Sato, F., Terada, S.: Genetically
837 encoded orientation probes for F-actin for fluorescence polarization microscopy.
838 *Microscopy* **68**(5) (2019) <https://doi.org/10.1093/jmicro/dfz022>
- 839 [56] Burghardt, T.P.: Time-resolved fluorescence polarization from ordered biological
840 assemblies. *Biophysical Journal* **48**(4), 623–631 (1985) [https://doi.org/10.1016/S0006-3495\(85\)83818-2](https://doi.org/10.1016/S0006-3495(85)83818-2)
841
- 842 [57] Suhling, K., Siegel, J., Lanigan, P.M.P., L ev eque-Fort, S., Webb, S.E.D., Phillips,
843 D., Davis, D.M., French, P.M.W.: Time-resolved fluorescence anisotropy imaging
844 applied to live cells. *Optics Letters* **29**(6), 584–586 (2004) <https://doi.org/10.1364/OL.29.000584>
845
- 846 [58] Volpato, A., Ollech, D., Alvelid, J., Damenti, M., M uller, B., York, A.G.,
847 Ingaramo, M., Testa, I.: Extending fluorescence anisotropy to large complexes
848 using reversibly switchable proteins. *Nature Biotechnology*, 1–8 (2022) <https://doi.org/10.1038/s41587-022-01489-7>
849
- 850 [59] Chan, F.T.S., Kaminski, C.F., Schierle, G.S.K.: HomoFRET fluorescence
851 anisotropy imaging as a tool to study molecular self-assembly in live cells.
852 *ChemPhysChem* **12**(3), 500–509 (2011) <https://doi.org/10.1002/cphc.201000833>
- 853 [60] Markwardt, M.L., Snell, N.E., Guo, M., Wu, Y., Christensen, R., Liu, H., Shroff,
854 H., Rizzo, M.A.: A genetically encoded biosensor strategy for quantifying non-
855 muscle myosin II phosphorylation dynamics in living cells and organisms. *Cell*
856 *Reports* **24**(4), 1060–10704 (2018) <https://doi.org/10.1016/j.celrep.2018.06.088>
- 857 [61] Bhatia, T., Husen, P., Brewer, J., Bagatolli, L.A., Hansen, P.L., Ipsen, J.H.,
858 Mouritsen, O.G.: Preparing giant unilamellar vesicles (GUVs) of complex lipid
859 mixtures on demand: Mixing small unilamellar vesicles of compositionally het-
860 erogeneous mixtures. *Biochimica et Biophysica Acta* **1848**(12), 3175–3180 (2015)
861 <https://doi.org/10.1016/j.bbamem.2015.09.020>
- 862 [62] Schmid, E.M., Richmond, D.L., Fletcher, D.A.: Reconstitution of proteins on elec-
863 troformed giant unilamellar vesicles. In: Ross, J., Marshall, W.F. (eds.) *Building*
864 *a Cell from Its Component Parts*. *Methods in Cell Biology*, vol. 128, pp. 319–338.
865 Academic Press, Cambridge, MA, USA (2015). <https://doi.org/10.1016/bs.mcb.2015.02.004>
866
- 867 [63] Abrahamsson, S., Chen, J., Hajj, B., Stallinga, S., Katsov, A.Y., Wisniewski,
868 J., Mizuguchi, G., Soule, P., Mueller, F., Darzacq, C.D., Darzacq, X., Wu, C.,
869 Bargmann, C.I., Agard, D.A., Dahan, M., Gustafsson, M.G.L.: Fast multicolor
870 3D imaging using aberration-corrected multifocus microscopy. *Nature Methods*
871 **10**, 60–63 (2012) <https://doi.org/10.1038/nmeth.2277>

- 872 [64] Yamaguchi, M., Goué, N., Igarashi, H., Ohtani, M., Nakano, Y., Mortimer, J.C.,
873 Nishikubo, N., Kubo, M., Katayama, Y., Kakegawa, K., Dupree, P., Demura, T.:
874 VASCULAR-RELATED NAC-DOMAIN6 and VASCULAR-RELATED NAC-
875 DOMAIN7 effectively induce transdifferentiation into xylem vessel elements under
876 control of an induction system. *Plant Physiology* **153**(3), 906–914 (2010) <https://doi.org/10.1104/pp.110.154013>
877
- 878 [65] Murata, T., Baskin, T.I.: Imaging the mitotic spindle by spinning disk microscopy
879 in tobacco suspension cultured cells. In: *Mitosis: Methods and Protocols*,
880 pp. 47–55. Springer, New York, NY, USA (2014). [https://doi.org/10.1007/](https://doi.org/10.1007/978-1-4939-0329-0_4)
881 [978-1-4939-0329-0_4](https://doi.org/10.1007/978-1-4939-0329-0_4)
- 882 [66] Thomas, J., Ingerfeld, M., Nair, H., Chauhan, S.S., Collings, D.A.: Pontamine
883 fast scarlet 4B: a new fluorescent dye for visualising cell wall organisation in
884 radiata pine tracheids. *Wood Science and Technology* **47**(1), 59–75 (2013) <https://doi.org/10.1007/s00226-012-0483-x>
885
- 886 [67] Nain, A.S., Sitti, M., Jacobson, A., Kowalewski, T., Amon, C.: Dry spin-
887 ning based spinneret based tunable engineered parameters (STEP) technique
888 for controlled and aligned deposition of polymeric nanofibers. *Macromolecular*
889 *Rapid Communications* **30**(16), 1406–1412 (2009) [https://doi.org/10.1002/marc.](https://doi.org/10.1002/marc.200900204)
890 [200900204](https://doi.org/10.1002/marc.200900204)
- 891 [68] Wang, J., Nain, A.S.: Suspended micro/nanofiber hierarchical biological scaffolds
892 fabricated using non-electrospinning STEP technique. *Langmuir* **30**(45), 13641–
893 13649 (2014) <https://doi.org/10.1021/la503011u>
- 894 [69] Jana, A., Tran, A., Gill, A., Kiepas, A., Kapania, R.K., Konstantopoulos,
895 K., Nain, A.S.: Sculpting rupture-free nuclear shapes in fibrous environ-
896 ments. *Advanced Science* **9**(25), 2203011 (2022) [https://doi.org/10.1002/advs.](https://doi.org/10.1002/advs.202203011)
897 [202203011](https://doi.org/10.1002/advs.202203011)
- 898 [70] Singh, J., Pagulayan, A., Camley, B.A., Nain, A.S.: Rules of contact inhibition
899 of locomotion for cells on suspended nanofibers. *Proceedings of the National*
900 *Academy of Sciences of the United States of America* **118**(12), 2011815118 (2021)
901 <https://doi.org/10.1073/pnas.2011815118>
- 902 [71] Padhi, A., Singh, K., Franco-Barraza, J., Marston, D.J., Cukierman, E., Hahn,
903 K.M., Kapania, R.K., Nain, A.S.: Force-exerting perpendicular lateral protrusions
904 in fibroblastic cell contraction. *Communications Biology* **3**(390), 1–11 (2020)
905 <https://doi.org/10.1038/s42003-020-01117-7>
- 906 [72] Garyfallidis, E., Brett, M., Amirbekian, B., Rokem, A., Van Der Walt, S.,
907 Descoteaux, M., Nimmo-Smith, I.: Dipy, a library for the analysis of diffusion
908 mri data. *Frontiers in Neuroinformatics* **8**, 71423 (2014) [https://doi.org/10.3389/](https://doi.org/10.3389/fninf.2014.00008)
909 [fninf.2014.00008](https://doi.org/10.3389/fninf.2014.00008)

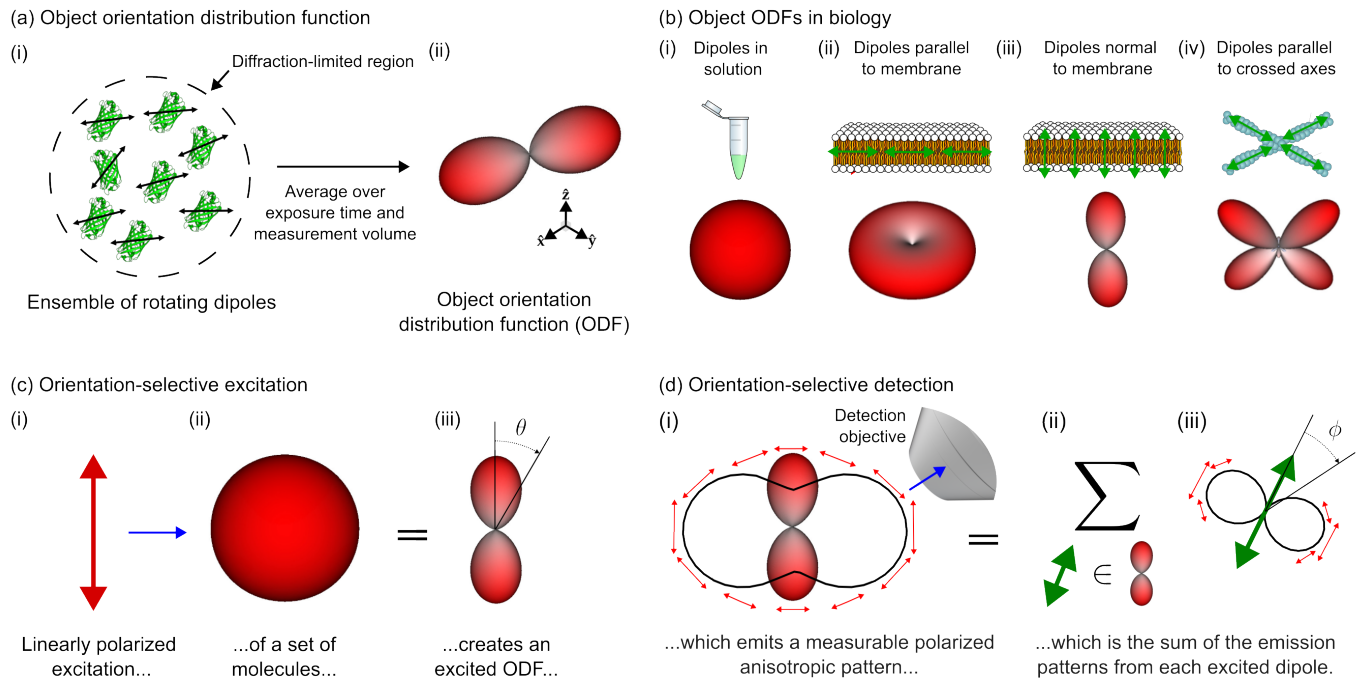
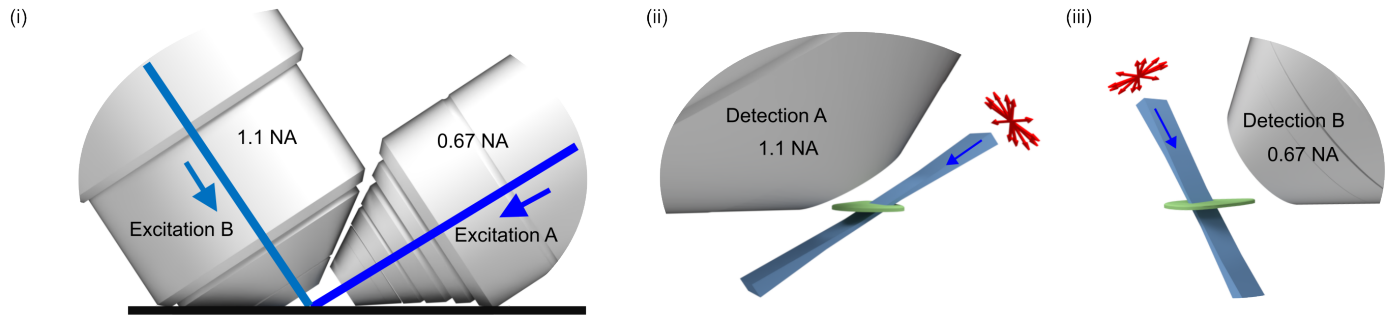
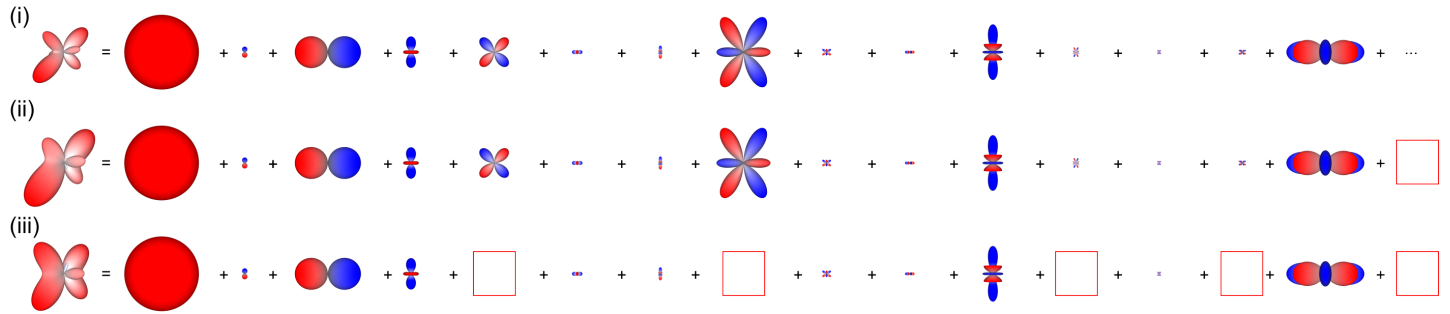


Fig. 1 Orientation distribution functions (ODFs) can model ensembles of oriented fluorophores that label biological structures, their excitation, and their detection. (a) (i) Fluorescent samples consist of molecules that move and rotate in three dimensions (e.g. green fluorescent protein molecules pictured), and many of the most common fluorescent molecules' excitation and emission behavior can be described by a single 3D dipole axis (double-sided black arrows overlaid on each molecule). Our instrument excites and measures emissions from diffraction-limited regions that contain many fluorescent molecules (dashed circle), so (ii) we simplify our model of individual emitters to a coarse-grained model called an object orientation distribution function (ODF). An ODF is a spherical function that we depict as a surface with a radius proportional to the number of dipoles in the measurement volume that are oriented along each direction. (b) Dipole distributions (top row) can be modelled by object ODFs (bottom row). (i) Fluorescent dipoles in solution typically rotate rapidly during the measurement time of fluorescent microscopes, so the corresponding ODFs are isotropic, depicted as a surface with constant radius. (ii-iv) When fluorescent dipoles (green double-sided arrows) are spatially and rotationally constrained, their corresponding object ODFs report the orientation of labelled biomolecules. (c) We can probe an object ODF by exciting a subset of molecules with polarized light. For example, when (i) linearly polarized light (red arrow) illuminates (blue arrow) an (ii) isotropic object ODF, (iii) the resulting subset of excited molecules, which we call an excited ODF, will have a $\cos^2 \theta$ dependence where θ is the angle between the incident polarization and the excitation dipole moment of the individual fluorophores in the distribution. Selectively exciting molecules creates contrast between different object ODFs. (d) We can create more contrast by selectively detecting an excited ODF's emissions. (i) An excited ODF (red glyph) emits a polarized emission pattern (red arrows, perpendicular to the emission direction) that is anisotropic (solid black line, radius is proportional to the emitted power along each direction) which encodes information about the excited ODF. Selectively detecting emissions with an objective (blue arrow) creates contrast between excited ODFs. (ii) The emission pattern in (i) is the sum (Σ) of the emissions from each dipole (green double-sided arrow) in (\in) the excited ODF. (iii) Similar to (i), each dipole emits a polarized emission pattern that is anisotropic, with each dipole emitting in a $\sin^2 \phi$ intensity pattern where ϕ is the angle between the emission dipole moment and the emission direction.

(a) Imaging overview



(b) ODFs decompose into weighted sums of spherical harmonics



(c) Simulation and reconstruction overview

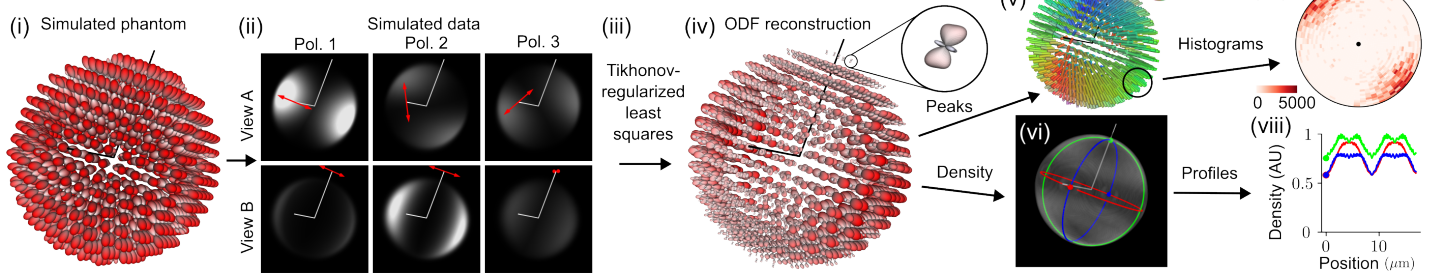


Fig. 2 Polarized dual-view inverted selective-plane illumination microscope (pol-diSPIM) data together with a physics-informed reconstruction enables volumetric measurement of three-dimensional orientation distribution functions. (a) (i) We imaged our samples with an asymmetric pair of objectives, each capable of excitation and detection. (ii) Illuminating our sample (green) with a light sheet (blue) from the 0.67 numerical aperture (NA) objective and detecting the emitted light from the 1.1 NA objective allows us to make planar measurements of diffraction-limited regions. Modulating the illumination polarization (red arrows) allows us to selectively excite ODFs within each diffraction-limited region, and orthogonal detection allows selective detection. (iii) Excitation from the 1.1 NA objective and detection from the 0.67 NA objective creates additional selective-excitation and selective-detection contrast and complementary spatial resolution. Scanning the sample through these polarized light sheets allows orientation-resolved volumetric acquisitions with more isotropic spatial resolution than detection from a single objective. (b) We used spherical harmonic decompositions of ODFs to simulate, reconstruct, and interpret our designs. (i) An example ODF is decomposed into the sum of an infinite number of spherical harmonics with the 15 smoothest non-zero terms shown. (ii) Truncating the infinite sum (red box at right) smooths the ODF while preserving its overall shape, demonstrating the angular resolution our instrument can recover. (iii) Removing more terms (five red boxes) distorts the ODF and increases its symmetry, demonstrating the effect of missing components in the spatio-angular transfer function. (c) (i) A simulated phantom of radially oriented ODFs on the surface of a sphere are used to (ii) simulate a dataset. Each volume is simulated with a different illumination objective (rows) and illumination polarization (columns, red arrows indicate polarization, Pol. = Polarization), illustrating how selective excitation and detection (with optical axes indicated by white lines) results in contrast that encodes spatio-angular information. (iii) A physics-informed reconstruction algorithm allows us to recover (iv) ODFs in volumetric regions (inset, a single ODF corresponding to a diffraction-limited volume). We reduce these reconstructions to lower-dimensional visualizations including (v) peak orientations, where the orientation and color of each cylinder indicates the direction along which most dipoles are oriented, and (vi) density, a scalar value indicating the total number of values within each voxel. We further summarize distributions of peak orientations with (vii) angular histograms, where the central dot indicates the viewing axis, and density with (viii) spatial profiles, where the colored profiles correspond to the circumferential profiles in (vi).

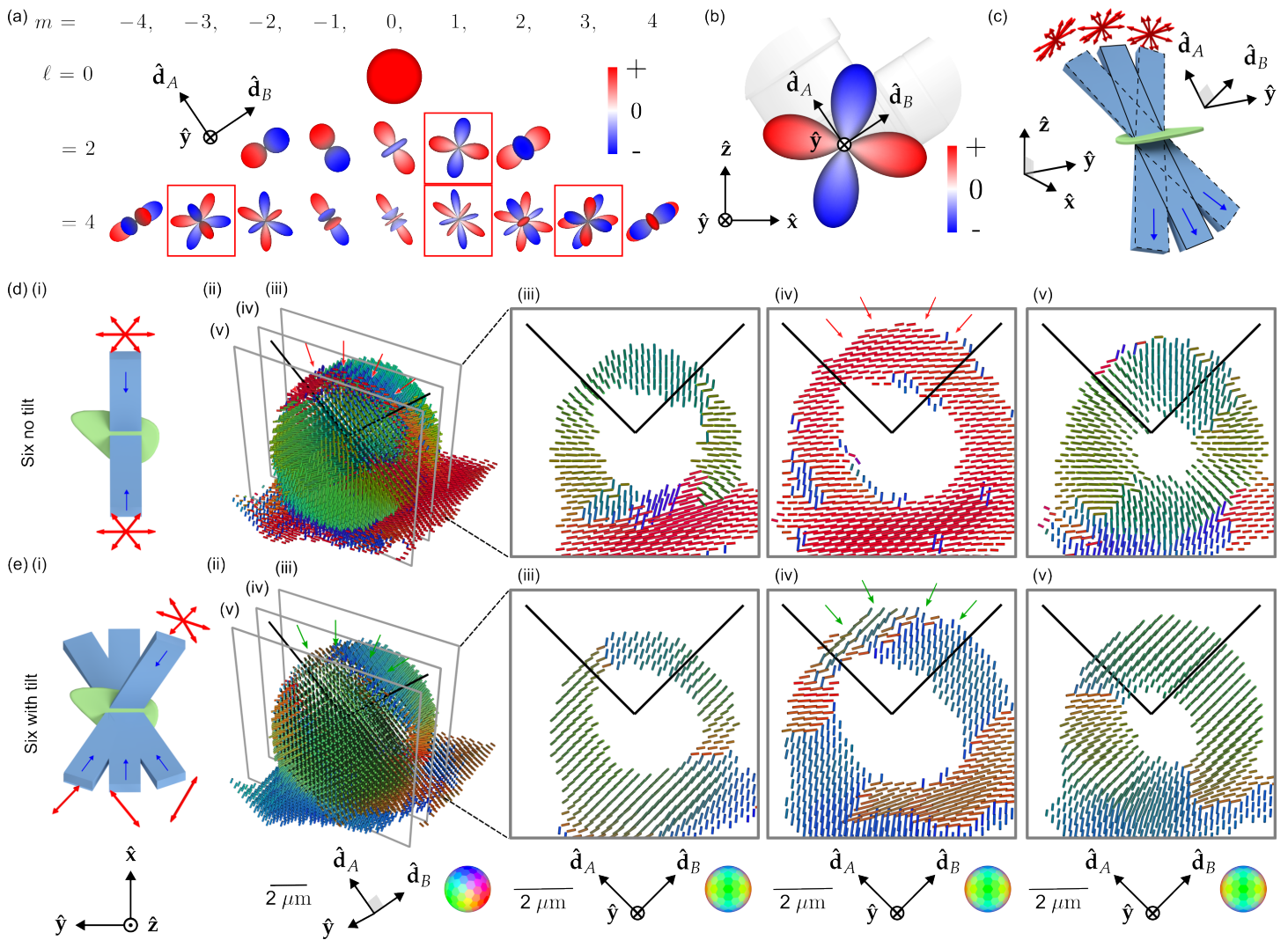


Fig. 3 Light-sheet tilting enables experimental recovery of second-order spherical harmonic coefficients and all peak orientations. (a) We found that our spatio-angular transfer function had “angular holes” when expressed in a basis of spherical harmonics aligned with the detection axes. Red boxes indicate null functions, spherical harmonics that are not passed to the detected data. (b) The second-order angular null function is particularly problematic because it prevents the completion of the $\ell = 2$ band, causing angular blind spots. Adding any multiple of an angular null function to the object creates identical data, so this angular null function is effectively invisible to our imaging system. (c) We added a MEMS mirrors to each excitation arm, enabling light-sheet illumination in the the typical straight-through configuration (blue rectangle with solid outline) and the new tilted configurations (blue rectangles with dashed outlines). Tilting the light sheet makes new polarization orientations (red arrows) accessible while illuminating the same positions in the sample. (d) (i) A schematic of our **Six no tilt** acquisition scheme, where the sample (green) is illuminated with light sheets (light blue) propagating parallel to the optical axes of the objectives (dark blue arrows) under three different polarization illuminations per light sheet (red arrows). (ii) Peak cylinder reconstruction from experimental data acquired from a giant-unilamellar vesicle (GUV), where color and orientation encodes the most frequent dipole orientation from within each voxel, spaced by 260 nm . We expect the dipole orientations to be everywhere normal to the GUV, but instead see a red stripe across the top of the reconstructed GUV (see red arrows). (iii-v) Slices through the peak cylinder reconstruction, with incorrect orientations marked with red arrows. (e) (i) A schematic of our **Six with tilt** acquisition scheme, which uses a view-asymmetric combination of polarization and tilted light sheets to acquire more angular information from six illumination samples. (ii-v) Peak cylinder reconstruction using tilted light sheets shows recovery of all peak orientations (see green arrows in (ii) and (iv)). Each column of (d) and (e) uses a single coordinate system described below the column where \hat{d}_A and \hat{d}_B are the detection optical axes.

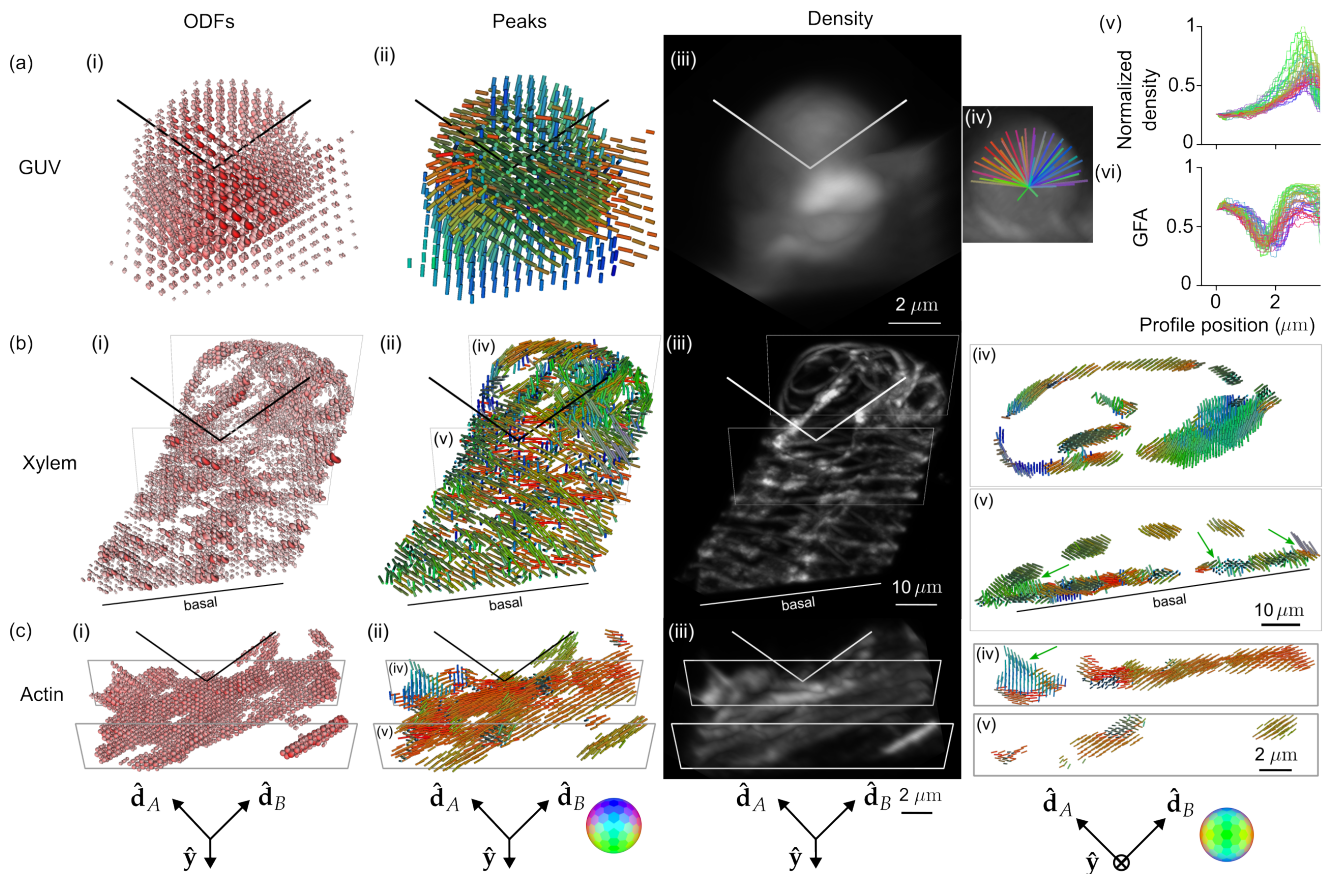


Fig. 4 Reconstruction of GUV, xylem, and actin samples validate pol-diSPIM's accuracy and extend known 2D orientation results to 3D. (a) A $\sim 6 \mu\text{m}$ -diameter GUV labelled with FM1-43 with (i) ODFs and (ii) peak cylinders separated by 650 nm . Radial profiles through the density map (iv) are used to plot density (v) and (vi) generalized fractional anisotropy (GFA) as a function of distance from the center of the GUV. (b) A xylem cell with its cellulose labelled by fast scarlet with (i) ODFs and (ii) peak cylinders separated by $1.56 \mu\text{m}$. Slices (iv, v) show peak cylinders separated by 650 nm and depict the dipole orientations tracking parallel to the helical cellulose structure, with different orientations on the basal and apical surfaces and spatially merging fibers distinguishable by their orientations (green arrows). (c) U2OS cells with actin labelled by phalloidin 488 with (i) ODFs and (ii) peak cylinders separated by 390 nm . Slices (iv, v) show peak cylinders separated by 260 nm and depict out-of-plane (green arrow) and variable in-plane orientations of fixed actin. Each column's camera orientation and orientation-to-color map is displayed in the bottom row. See also, **Supplemental Movies M1–6**.

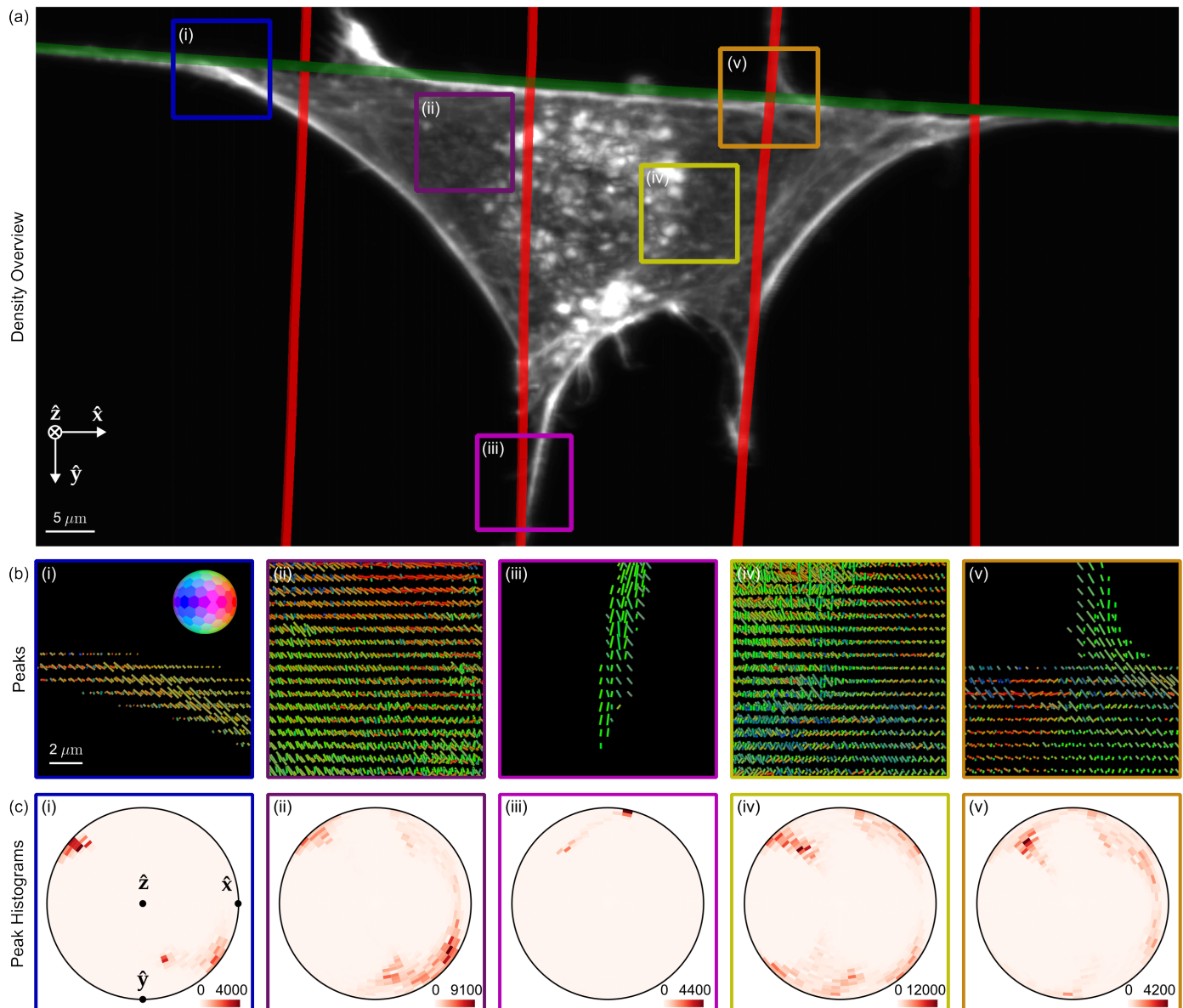


Fig. 5 pol-diSPIM measurements of phalloidin-labelled 3T3 mouse fibroblasts grown on nanowires show dipoles oriented parallel to their nearest nanowires and reveal distinct out-of-plane dipole populations across the cell. (a) Reconstructed density maximum intensity projection of a cell grown on crossed nanowires, with hand-annotated wires measured from a wire-specific channel highlighted with red and green lines. ROIs (i-iii) are outlined in color and examined in subsequent panels. (b) Peak cylinders drawn every 780 nm in regions with total counts > 5000, colored by orientation (see inset color hemisphere), with lengths proportional to the maximum diameter of the corresponding ODF. (c) Histogram of all peak cylinders with total counts > 5000 in each ROI. Bins near the edge of the circle indicate in-plane orientations, bins near the center indicate out-of-plane orientations, and dots mark the Cartesian axes on the histogram.

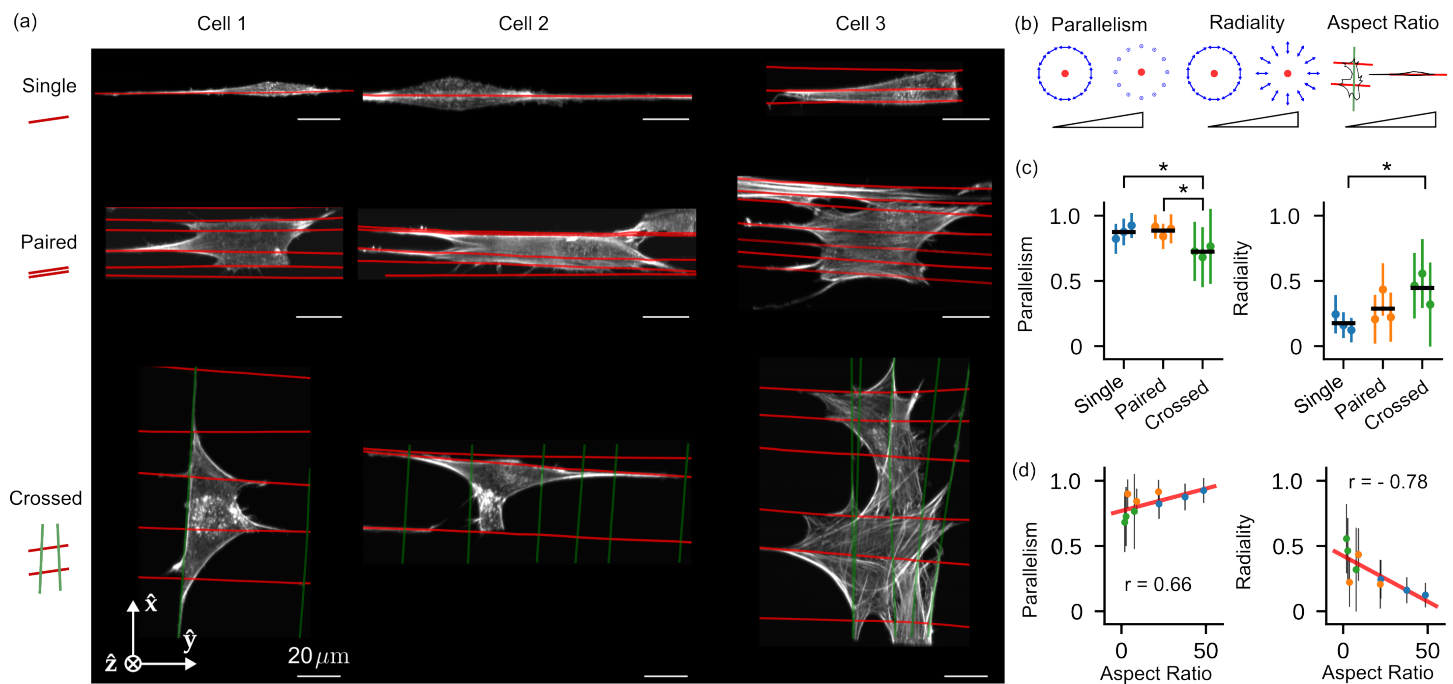


Fig. 6 Measurements of 3T3 mouse fibroblasts grown on different nanowire arrangements show correlations between voxel- and cell-scale orientations. (a) Reconstructed density maximum intensity projections of three cell repeats (columns) grown on varying nanowire arrangements (rows) named "Single", "Paired", and "Crossed" (cartoons at left). Wires are overlaid as red and green lines. (b) We collected reconstructed peak directions in voxels that were $< 5 \mu\text{m}$ from a wire and had total counts > 5000 , calculated their parallelism and radiality with respect to their nearest wire (see inset cartoons where the red dot indicates a wire, and blue arrows indicate the neighboring peak directions for strongly parallel and radial peaks), and plotted their mean (dots) and standard deviation (error bars) for each cell and nanowire arrangement (colors). Additionally, we calculated each cell's "Aspect Ratio", the ratio of the largest and smallest eigenvalues of the cell's moment of inertia tensor (with the reconstructed density as a proxy for mass). (c) We compared population means (horizontal black lines) with a t -test and marked $p < 0.05$ - significant differences with asterisks. (d) We compared our local voxel-wise parallelism and radiality metrics to the cell's global aspect ratio. We found positive and negative correlations between the aspect ratio and the parallelism and radiality, respectively, indicating local-global correlations in cellular behavior. Colored dots match (c), the red line is a linear fit to all nine data points, and the annotated r values are Pearson correlation coefficients.